Journal of Hydrology 612 (2022) 128275

Contents lists available at ScienceDirect

Journal of Hydrology

journal homepage: www.elsevier.com/locate/jhydrol

Research papers

Past and future terrestrial water storage changes in the lower Mekong River basin: The influences of climatic and non-climatic factors

Jinghua Xiong [a], Shenglian Guo [a,*], Deliang Chen [b], Yulong Zhong [c], Bingshi Liu [d], Abhishek [e], Jiabo Yin [a]

[a] State Key Laboratory of Water Resources and Hydropower Engineering Science, Wuhan University, Wuhan 430072, Hubei, China
[b] Department of Earth Sciences, University of Gothenburg, Gothenburg 405 30, Sweden
[c] School of Geography and Information Engineering, China University of Geosciences (Wuhan), Wuhan 430079, Hubei, China
[d] School of Geodesy and Geomatics, Wuhan University, Wuhan, China
[e] School of Environment and Society, Tokyo Institute of Technology, Yokohama 226-8503, Japan

ARTICLE INFO

Keywords:
Terrestrial water storage
Climate variability and change
Human activities
Future projection
Lower Mekong River basin

ABSTRACT

Climate change and human activity such as reservoir operation have altered the hydrological system in the transboundary Mekong River basin (MRB) over decades, urging a need to assess the historical changes and future projections of freshwater availability. Here we examined changes of terrestrial water storage anomalies (TWSA) from the Gravity Recovery and Climate Experiment satellites in the lower MRB during 2003–2020, and subsequently partitioned and attributed them into climate-driven and non-climate-driven components using the WaterGAP hydrological model (WGHM) with and without consideration of human activities, together with a statistical method driven by climatic forcing only. Further, integrated future TWSA was projected under different climate change scenarios during 2030–2099 forced with four downscaled and bias-corrected simulations of four global climate models. Results show a decreasing TWSA trend of −3.7 ± 1.8 mm/a during 2003–2020. The WGHM-based climate-driven TWSA, which is highly correlated with the statistical modeling results, and non-climate-driven part suggests a trend of −0.3 ± 1.4 and 0.01 ± 0.07 mm/a during 2003–2016, respectively. The climate-driven TWSA is well explained by the changes in decreasing precipitation (−1.3 ± 8.5 mm/a) and increasing air temperature (0.05 ± 0.02 ℃/a) spatially and temporally, while the non-climate-driven component is closely linked to human activities such as growing sectoral human withdrawal (0.13 ± 0.14 mm/a), increasing reservoir regulation (0.01 ± 0.08 mm/a), and changing land cover. TWSA under future climate changes is projected to increase from 9.3 ± 21.4 to 12.2 ± 12.2 mm and from 1.6 ± 41.2 to 12.3 ± 30 mm in the near (2040–2059) and far future (2080–2099) under various scenarios comparing with the historical period (2003–2020). Future flood potential, estimated with TWSA and precipitation, was also projected to increase. This study provides important inferences for decision-makers and stakeholders to better understand the water cycle and manage water resources in a changing environment.

1. Introduction

Terrestrial water storage (TWS), which is summed from water stored in rivers, lakes and reservoirs, soil, groundwater systems, snow and glaciers, and vegetation, is a crucial variable in the global hydrological cycle and land–atmosphere interaction processes (Rodell et al., 2018). As an effective indicator of regional water balance or imbalance (Abhishek et al., 2021), natural hazards such as floods and droughts (Abhishek and Kinouchi, 2022), terrestrial carbon uptake (Humphrey et al., 2018), ice sheets and glaciers mass fluctuations (van den Broeke et al., 2009), and sea-level rise (Eicker et al., 2016), TWS changes play a determining role in modulating water flux interactions within various Earth system components (Pokhrel et al., 2021). Nevertheless, global variations in TWS are still inadequately known due to the paucity of field observation gauges worldwide and considerable uncertainties in hydrological and land surface models (Scanlon et al., 2018), particularly in the international river basins with restricted data sharing policies and intensive water conflicts among different countries. As one of the most

* Corresponding author.
E-mail address: slguo@whu.edu.cn (S. Guo).

https://doi.org/10.1016/j.jhydrol.2022.128275
Received 6 June 2022; Received in revised form 17 July 2022; Accepted 23 July 2022
Available online 4 August 2022

important international rivers of Asia, the Mekong River flowing across six countries, including China, Myanmar, Lao, Thailand, Vietnam, and Cambodia, feeds approximately 70 million inhabitants and sustains crops, livestock, and the ecosystem of the basin (Yun et al., 2021a). Under the background of emerging freshwater availability, monitoring TWS changes in the Mekong River basin (MRB) is of great importance to address the comprehensive cooperation in regional water resources management and development (Jing et al., 2020; Liu et al., 2022).

Jointly developed by the National Aeronautics and Space Administration and the German Aerospace Center, the Gravity Recovery and Climate Experiment (GRACE) mission that launched in March 2002 can provide monthly terrestrial water storage anomaly (TWSA) worldwide with unprecedented accuracy by measuring distance changes between the twin satellites (Tapley et al., 2019). After its decommissioning in June 2017, the GRACE Follow-On (also referred to as GRACE hereafter) satellites commissioned in May 2018, have continued to assess global TWSA changes up to the present. The GRACE satellites have enabled the investigation of spatiotemporal variability of TWSA on multiple temporal (from seasonal to decadal) and spatial (from regional to global) scales (Humphrey et al., 2016; Sun et al., 2020; Guo et al., 2021). A few studies have attempted to reveal TWSA changes in the MRB (Pham-Duc et al., 2019; Jing et al., 2020; Bibi et al., 2021). Specifically, Jing et al. (2020) used five different GRACE solutions and found a downward trend with trends ranging from 0.0 to −14.5 mm/a between 2002 and 2016 in the upper reach ($p < 0.05$), while there were no statistically significant trends in the lower basin. Moreover, Bibi et al. (2021) examined the TWSA changes in the upstream region and also discovered significant ($p < 0.05$) negative trends at rates ranging from −3.3 to −5.9 mm/a during 2002–2016 based on multiple GRACE solutions.

Climate change has significantly altered the hydrological system of the MRB over decades, which is mainly reflected by the variations in precipitation and temperature (Nie et al., 2018; Gao et al., 2019). In addition, the growing food demands, rapid population expansion, and dramatic urban development have resulted in massive changes in land use/land cover (LUCC), alteration of the hydrological cycle, and development of hydropower systems throughout the basin (Johnston and Kummu, 2012; Liu et al., 2021). Therefore, both climate and non-climate factors should have played a role in the historical TWSA changes in the MRB. Therefore, the quantification of the respective contributions of the two factors to the total change in the past TWSA is crucial but remains unexamined.

Most of the previous studies merely focused on the historical changes of TWSA in the MRB due to the relatively short period (~21 years) of the GRACE missions, while the future projections under the combined effects of both climatic and non-climatic factors remain rarely examined. There are generally-two categories of methods to obtain future TWSA. The first group relies on physically-based models to describe changes in climate, land surface, and hydrology. As an example, Pokhrel et al. (2021) forced a large ensemble of global hydrological models (GHMs), land surface models (LSMs), and dynamic global vegetation models (DGVMs) using four different global climate models (GCMs) from Coupled Model Intercomparison Project Phase 5 (CMIP5), and acquired global TWSA projections under distinctive emission scenarios for drought possibility evaluation until the end of the 21st century. This method has been used to assess the great potential of the combination of GCMs and GHMs/LSMs/DGVMs to simulate the future TWSA (Oki and Kanae, 2006; Schewe et al., 2014). Xiong et al. (2022) directly used the original GRACE observations to perform the bias correction for the TWSA simulations of multiple GCMs from the CMIP6 archive and subsequently applied this approach to assess the future TWSA and associated flood potential changes in the Yangtze River basin. However, the systematic analysis of projected TWSA in the MRB is still unexplored using either kind of the above-introduced methods.

Therefore, the main objectives of this study are (1) to investigate the spatiotemporal variability of climate-driven and non-climate-driven TWSA contributions as well as their influential factors over the lower MRB during the historical period 2003–2020; (2) to project the future changes of TWSA that are jointly affected by both climate and non-climate factors under multiple scenarios during the future period 2030–2099.

2. Data and methods

2.1. Study area

We selected the lower MRB as the study region because the shape of upstream MRB is very narrow and elongated, thus it is very likely that GRACE signals possess leakage errors, i.e., contamination (gain/loss) in the target signal from the surrounding region (e.g., glacier melting on the Qinghai-Tibet Plateau (Chao et al., 2020)). Located within the domain of 9°48′–22°42′N and 99°51′–108°42′E, the lower MRB has a total area of ~ 606,000 km^2, occupying ~ 77 % of the whole of MRB with a total area of ~ 795,000 km^2 (see Fig. 1). The lower MRB is shared by five countries in Southeast Asia including Laos, Thailand, Vietnam, Cambodia, and Myanmar. Dominated by the tropical rainforest climate and tropical monsoon climate, more than 80 % of precipitation in the basin occurs in the wet season (from June to November) while only ~ 20 % is received during the dry season (from December to May) (Yun et al., 2021b). The cropland is the main land use type and more than 10 million hectares of cultivated land are employed for rice production (Jing et al., 2020).

The lower MRB has experienced significant climate changes since the 1980s, which were mainly reflected by the warming at a rate higher than the global average warming rate and increasing annual precipitation (Kingston et al., 2011; Fan and He, 2015). In addition, future projections of air temperature are expected to steadily increase up to the end of the 21st century, with the annual precipitation continuing to grow under multiple scenarios (Västilä et al., 2010; Kingston et al., 2011). The lower MRB feeding more than 60 million people (status: 2010, You et al.,

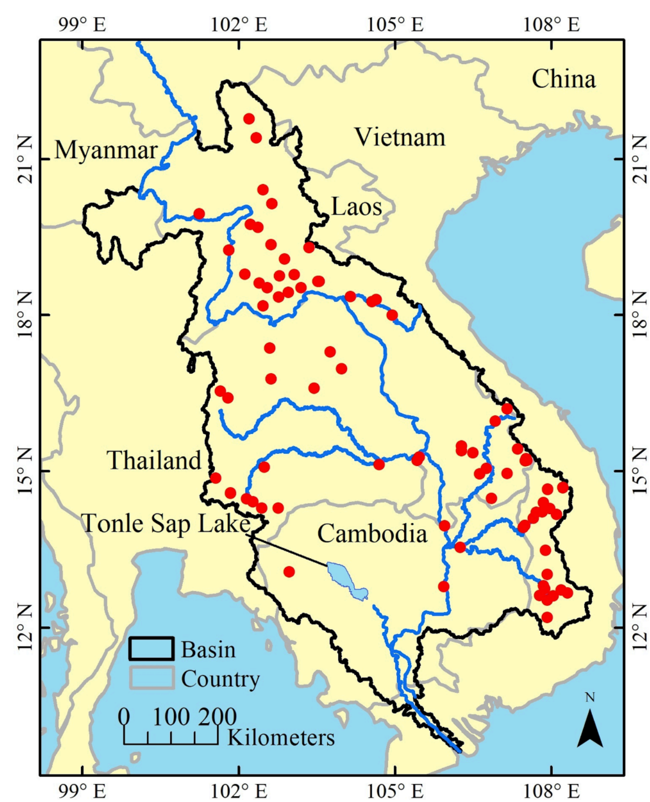

Fig. 1. Location of the lower Mekong River basin. Note: The red circles represent the operational reservoirs, whose basic information (location, function, year of completion, height and total storage capacity) is listed in Table S1.

2014) is heavily irrigated for agriculture purposes, and the population is projected to grow by 60 % by 2050 compared to its 2005 values (Pech and Sunada, 2008). Therefore, the growing demand for water and energy resources due to population and urban expansion has led to over 79 large reservoirs in operation with a total storage capacity of 57.5 km^3 up to the year 2021 (Fig. 1). The detailed information on these operational reservoirs is listed in Table S1. The statistics of the operational reservoirs are provided by a recent study (Yun et al., 2021a). Therefore, the increasingly evident climate and non-climate changes highlight the urgent need to understand the TWSA changes in both the past and future.

2.2. GRACE TWSA

We used the GRACE mass concentration block (mascon) data during 2003–2020 to assess the TWSA changes in the lower MRB, which was produced by the Center for Space Research at the University of Texas at Austin (CSR) (Watkins et al., 2015; Save et al., 2016) (Table S2). The mascon solutions are derived by parameterizing the gravity field with regional mass concentration functions. Unlike the conventionally used spherical harmonics GRACE products, the mascon solutions are free from leakage signals and several categories of post-processing errors such as de-correlated and de-stripping noises (Scanlon et al., 2016; Wiese et al., 2016). Covering the period 2003–2020, the monthly mascon solutions have been resampled to a common 0.5° spatial resolution. The mascon data represents the TWSA relative to the average gravity field between 2004 and 2009. A total of 22 missing months due to instrumental issues and an 11-month data gap between two generations of GRACE satellites (from July 2017 to May 2018) are filled with a recently published GRACE reconstructions dataset (Li et al., 2021), which is also trained with the CSR mascon solution based on multiple climatic/hydrological variables and a combination of machine learning and statistical decomposition techniques. Since no calibration processes are needed across the missions and the precision and spatiotemporal sampling are equivalent, there are no existing intermission biases between GRACE and GRACE Follow-On satellites (Landerer et al., 2020). To investigate the influences of distinctive constraints and the scale of the grid cells from different processing institutions, the mascon solution from the NASA Jet Propulsion Laboratory (JPL) agency is also used for comparison. Similarly, the missing months and the data gap are filled with a recent GRACE reconstructions dataset trained with the JPL mascon solution (Mo et al., 2021), which is derived using the Bayesian deep learning method combined with ERA5-Land reanalysis. The comparisons between the continuous CSR and JPL mascon solutions on the basin and grid scales suggest high consistency with the correlation coefficient of 0.99 (Fig. S1), highlighting the negligible influences of divergent GRACE solutions.

2.3. Decomposition of TWSA

The WaterGAP (v-2.2d) hydrological model (WGHM) (Eicker et al., 2014; Schmied et al., 2021) was applied to decompose the TWSA into climate- and non-climate-driven parts from the period 2003–2016. The WGHM is a state-of-the-art hydrological model that simulates the full components of TWSA including water stored in river, snow, lakes and reservoirs, soil, aquifers, and vegetation over non-glacierized regions. Forced by the "WATCH Forcing Data methodology applied to ERA-Interim data" (WFDEI) dataset, it provides direct human intervention with hydrological cycle such as irrigation, reservoir regulation, and groundwater extraction (Weedon et al., 2014; Schmied et al., 2021). The WGHM model has been widely employed in regional and global hydrology research (An et al., 2021; Hosseini-Moghari et al., 2020). We also used simulations of the surface water, groundwater, and soil moisture storage from the WGHM to investigate the variations of different components of TWSA. The climate-driven TWSA is estimated using the "nosoc" mode of the WGHM, which did not account for direct human activities such as irrigation and reservoir management.

In addition, a recently proposed statistical method (Liu et al., 2021) which has been validated over major global river basins, was also applied to identify the climate-driven TWSA for comparison and independent check. This method can reconstruct both seasonal and non-seasonal signals in climate-driven TWSA using precipitation and air temperature data, which were also derived from the WFDEI meteorological dataset in our study. Moreover, several widely used climate forcing products such as ERA5, CRU TS (v-4.05), and GLDAS (-v2.1) were retrieved to detect the uncertainty sourced from different climate inputs (Table S2). Then, we subtract the naturalized WGHM simulations (i.e., "nosoc" mode) from the standard WGHM outputs (i.e., "histoc" mode) to estimate the non-climate-driven TWSA, which has considered both climate and human factors (Huang et al., 2015; Xie et al., 2019). Similarly, we also estimated the non-climate-driven TWSA by removing the statistically reconstructed climate-driven TWSA from the GRACE TWSA for comparison (Zhong et al., 2019). The training/testing configurations and the optimized parameters of the statistical method have been summarized in Table S3.

2.4. Projected TWSA

The WGHM was applied to assess the future TWSA changes under the joint effects of climate- and non-climate factors during the period 2030–2099, with a uniform spatial resolution of 0.5°. The meteorological forcing data, including precipitation, air temperature, solar radiation, wind speed, specific humidity, and surface pressure, generated from four GCMs (i.e., GFDL-ESM2M, HadGEM2-ES, IPSL-CM5A-LR, and MIROC5) of the CMIP5 archive, have undergone statistical downscaling and bias correction using the Inter-Sectoral Impact Model Intercomparison Project (ISI-MIP) methods (Hempel et al., 2013; Lange, 2018, 2019). Three future scenarios are considered for each GCM, including a low (RCP2.6), a medium–high (RCP6.0), and a high (RCP8.5) greenhouse gas concentration scenario, and are subsequently divided into near (2040–2059) and far (2080–2099) future periods for comparison. The projected precipitation and air temperature were also derived to analyze the future changes in climatic factors. Furthermore, we also calculated a Flood Potential Index (FPI) using the projected TWSA and precipitation to evaluate the future changes in flood probability over the lower MRB, which were compared with the historical period during 2003–2020. FPI was initially introduced by Reager and Famiglietti (2009) and has been widely used in the GRACE community to represent the large-scale flood possibility (Zhu and Yuan, 2021). Higher FPI (<1) can generally be translated into a greater flood potential, and vice versa. All the simulations are conducted under the framework of phase 2b of the ISI-MIP project (Warszawski et al., 2014). The applicability of the future projections of TWSA has been fully evaluated in a recent global study (Pokhrel et al., 2021).

2.5. Auxiliary data

Multi-source data from the remote sensing, reanalysis, and models were collected to analyze the climatic and non-climatic variables influencing the TWSA. Specifically, precipitation and air temperature from the WFDEI meteorological dataset were used to study the climate variability during 2003–2016, which is consistent with the WGHM model (Weedon et al., 2014). However, the FPI between 2003 and 2020 was derived based on GRACE TWSA and ERA5 precipitation data due to the unavailability of the WFDEI product after 2016. The comparisons among different precipitation datasets show satisfactory agreement in the lower MRB, suggesting an insignificant uncertainty in the choices of precipitation datasets (Fig. S2). ERA5 reanalysis dataset is the 5th generation atmospheric reanalysis of the global atmosphere produced by the Copernicus Climate Change Service at the European Centre for Medium-Range Weather Forecasts (ECMWF). Further, the ERA5-land product provides a consistent view of land variables from 1950-present at an enhanced resolution compared to ERA5 over global land, based on the 4D-Var assimilation scheme, Integrated Forecast system model-41r2, and HTESSEL land surface model driven by meteorological forcing from the ERA-Interim atmospheric reanalysis and precipitation adjustments based on the Global Precipitation Climatology Project (GPCP) data (Hersbach et al., 2020). Further, the monthly remote sensing Normalized Difference Vegetation Index (NDVI) from the Moderate Resolution Imaging Spectroradiometer (MODIS-13C2) product was obtained to assess the influence of land cover on TWSA, which was also validated based on the yearly satellite-based land cover map retrieved from the ESA CCI (climate change initiative) project (ESA, 2017).

Two global irrigation datasets from the Food and Agriculture Organization (FAO) and Nagaraj et al. (2021) were utilized to assess the changes in the irritation area. The basic information on dams and reservoirs in the lower MRB from Yun et al. (2021a) was collected to investigate the changes in man-made hydrologic constructions. Similarly, simulated reservoir storage from the WGHM was also collected for attribution analysis. The monthly actual total consumptive water use, as the sum of abstracted water from surface water and groundwater in the WGHM model (Schmied et al., 2021), was also used for the interpretation of human water use.

We also obtained a global gridded reconstruction of water withdrawal for sectoral water use including irrigation, domestic, electricity generation, livestock, mining, and manufacturing during 2003–2010 from Huang et al. (2018) for comparison. The irrigation withdrawals are derived from four optimized GHMs, including the WGHM, PCR-GLOBWB, LPJmL, and H08 models, of which the WGHM was selected for consistency in this study. Finally, we obtained the satellite-based water level and surface area time series during 2003–2020 in the largest freshwater lake in South East Asia, the Tonle Sap Lake, to validate our examinations of TWSA variations given its significant role in regulating the flows in the MRB (Campbell et al., 2009; Wang et al., 2020; Chen et al., 2021). Therefore, the monthly water volume changes were estimated according to Taube (2000), which has been widely used in lake volume change (Zhang et al., 2017, 2019, 2021).

2.6. Uncertainty Estimation

Various methods were applied to quantify the uncertainties inevitably embedded in and propagated from the multisource data used. Specifically, the uncertainty in the CSR mascon solution was estimated as the residuals after removing the long-term trends and seasonal (annual and semi-annual) signals from the raw series (Scanlon et al., 2016). Moreover, the uncertainty in the WGHM simulations under “nosoc” and “histsoc” modes was calculated as the 10 % range (i.e., 90 % to 110 % of modeling results) (Schmied et al., 2021). The uncertainty in the statistically reconstructed climate-driven TWSA was taken as one standard deviation of 20,000 equally acceptable samples from MCMC simulation when training the model (Liu et al., 2021). Consequently, the non-climate-driven TWSA from both the WGHM and the statistical method were estimated as the square root of the sum of squares of uncertainty in WGHM (“histsoc” mode) and GRACE data, respectively. Moreover, the uncertainty of long-term trends in TWSA can be calculated as one standard deviation of the linear regression with a significance level of 0.95 (*t*-test), which was estimated using the linear regression method for the yearly average time series.

Given the substantial uncertainties in future TWSA projections sourced from four meteorological forcings (i.e., GFDL-ESM2M, HadGEM2-ES, IPSL-CM5A-LR, and MIROC5), the generalized three-cornered hat (GTCH) method was employed to estimate their respective uncertainty during 2030–2099. The GTCH method estimates the relative covariance of different sets of TWSA projections among at least three datasets, without the need for any prior knowledge information (Premoli and Tavella, 1993). It has been broadly used in estimating TWSA uncertainty from both GRACE and models globally due to its high effectiveness and robustness (Long et al., 2014, 2017). Moreover, we fused different categories of TWSA projections using the weighted averaging method, in which the corresponding weights of various TWSA datasets were determined based on the relative variance estimated by the GTCH method under the assumption of no correlations with each other (Yan et al., 2021). We also compared the fused projections and the ensemble mean to constrain the uncertainty.

3. Results

3.1. Historical TWSA variations

Fig. 2 illustrates the monthly time series of TWSA, climate-driven, and non-climate-driven during the period 2003–2020, and their annual cycles are presented in Fig. S3. GRACE data generally ranges from −300 to 300 mm except for the extremely high value in the wet season of 2011. The overall negligible uncertainty of GRACE TWSA is found (grey shaded regions), with relatively higher values in the 11-month data gap between July 2017 and May 2018. Larger uncertainties in the peaks and troughs compared with other occasions are apparent. As a result of both climate and non-climate factors, the GRACE TWSA has a downward rate of -3.7 ± 1.8 mm/a, similar to the trend (-3.3 ± 2.2 mm/a) during the period 2003–2016. Moreover, consistent changes in WGHM TWSA with GRACE results are detected, with relatively low amplitude and high uncertainty. Therefore, an underestimated trend of -0.3 ± 1.4 mm/a is discovered during 2003–2016 compared to the GRACE data, which are mainly caused by the decrease in groundwater (-0.2 ± 0.4 mm/a) and surface water storage (-0.2 ± 0.6 mm/a) (Fig. S4). The identified climate-driven TWSA from the WGHM and statistical model in the lower MRB are shown in Fig. 2. The naturalized WGHM-modeled TWSA illustrates close agreement with the statistically reconstructed climate-driven TWSA based on different climate forcings, with the respective correlation coefficient of 0.89 (WFDEI), 0.81 (ERA5), 0.91 (CRU TS), and 0.89 (GLDAS), highlighting the robustness of WGHM under the natural mode. Climte-driven TWSA and GRACE TWSA share similar seasonal features that peak in September/October while reacheing the lowest in April/May, which may be connected to the tropical monsoonal climate that is dominated by the Southwest Monsoon (Fig. S3). However, there are considerable uncertainties in the reconstructed climate-driven TWSA, especially for the WFDEI and ERA5 forcings. The comparatively better performance of the CRU TS and GLDAS forcing might be caused by the integration of the in-situ observations and remote sensing products. It indicates that different climate forcings might produce various uncertainties in the climatic reconstructions, and the lack of consideration of inflow from the Lancang River basin will inevitably introduce some uncertainty. Consequently, divergent trends of climate-driven TWSA from the WGHM (-0.3 ± 1.4 mm/a) and statistical model are seen during 2003–2016, which widely range from -3 ± 3.6 (CRU TS) and 6.7 ± 5.9 (ERA5) mm/a. In terms of non-climate-driven changes in TWSA, substantial differences are determined from the statistical model due to the propagated uncertainties in GRACE and climate-driven TWSA and multiple datasets of meteorological forcing, causing the trends ranging from -10 ± 4.6 (ERA5) and -0.3 ± 2.4 (CRU TS) mm/a during 2003–2016. Similarly, WGHM-based non-climate-driven TWSA presents a pattern that non-climate-driven TWSA is dominated by the spread of data uncertainty, with relatively low amplitude and trend between 2003 and 2016 (0.01 ± 0.07 mm/a) (Fig. S5). Therefore, despite the large uncertainty sourced from the different models and forcings, we conclude that the trends in TWSA from 2003 to 2016/2020 are primarily governed by the climate-driven components with a limited contribution from the non-climate-driven changes. The limited influence of the non-climate-driven TWSA can be explained by the fact that despite a large number of dam reservoir constructions (Table S1), their total capacities (~95 mm of equivalent water depth in 2020) are one order of magnitude less than the TWSA amplitude variations (~800 mm). Also, the groundwater pumping in the lower MRB might have been small owing to the abundant precipitation and surface water resources, the latter of

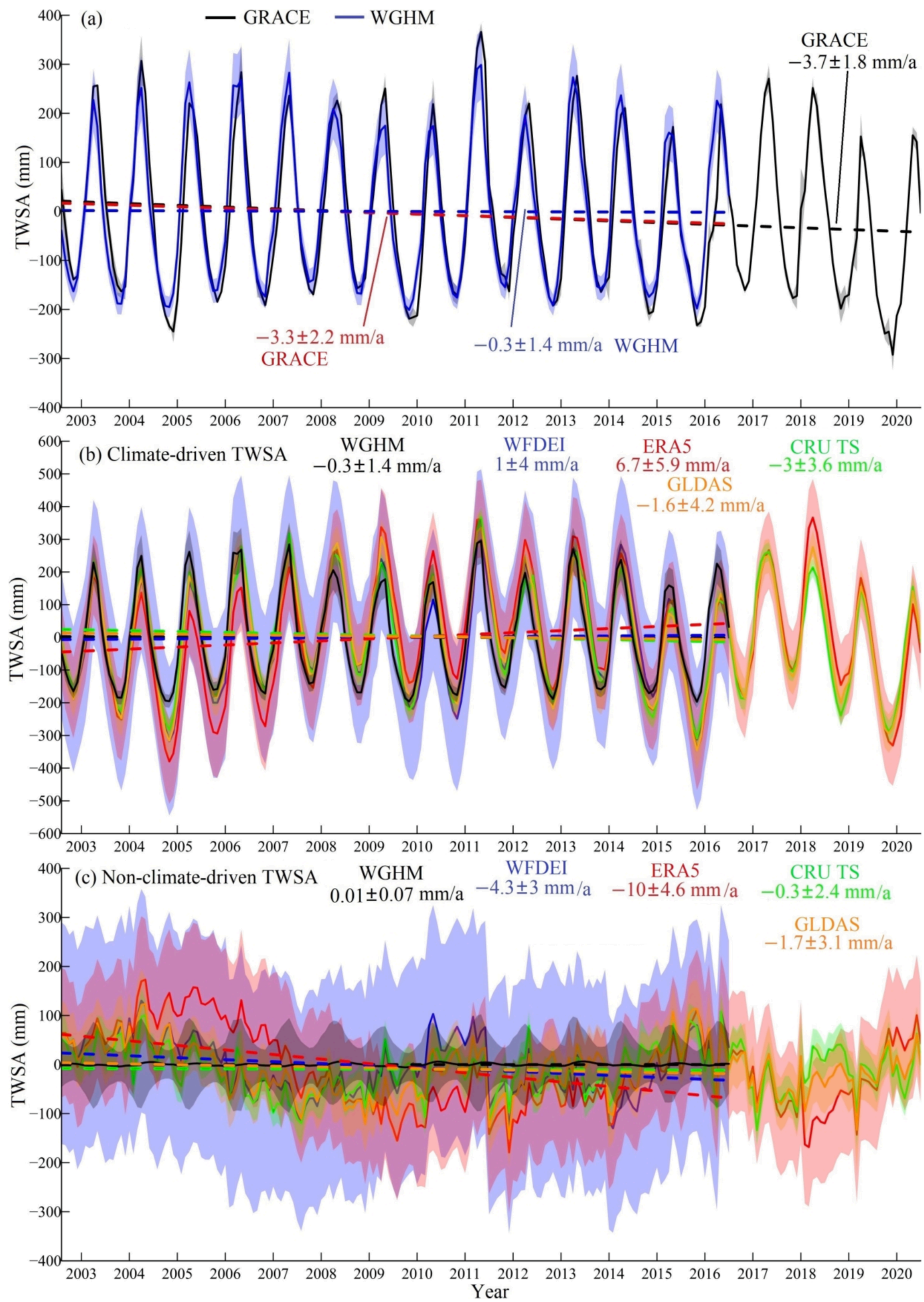

Fig. 2. Time series and trends of (a) TWSA, (b) climate-driven TWSA, and (c) non-climate-driven TWSA from the GRACE, WGHM, and statistical model in the lower MRB during 2003–2020. The shaded regions indicate the uncertainties of different variables. Please refer to section 2.6. "Uncertainty Estimation" for the details.

which contributes ~ 40–45 % of TWSA changes (Pham-Duc et al., 2019).

Fig. 3 demonstrates the spatial distribution of trends in TWSA, climate-driven TWSA, and non-climate-driven TWSA during 2003–2016/2020. For the period 2003–2020. The majority of the lower MRB illustrates overall TWSA depletion trends ($p < 0.05$) except for the northern region where TWSA increases from 2 to 8 mm/a with the uncertainties of ~ 3 mm/a. In addition, GRACE observations show significant ($p < 0.05$) decreasing trends with rates ranging from −16.0 to −8.0 mm/a over the western and southern parts of the basin, and the uncertainties generally fluctuate between 2.0 and 4.0 mm/a. Furthermore, satellite-based water levels from multi-source altimetry sensors and water surface area from different optical imageries of the largest inland water body, i.e., Tonle Sap Lake in Cambodia, are demonstrated in Fig. S6. It can be seen that water surface area, water level, and derived water volume changes show downward trends during the period 2003–2020, agreeing well with GRACE observations. A similar

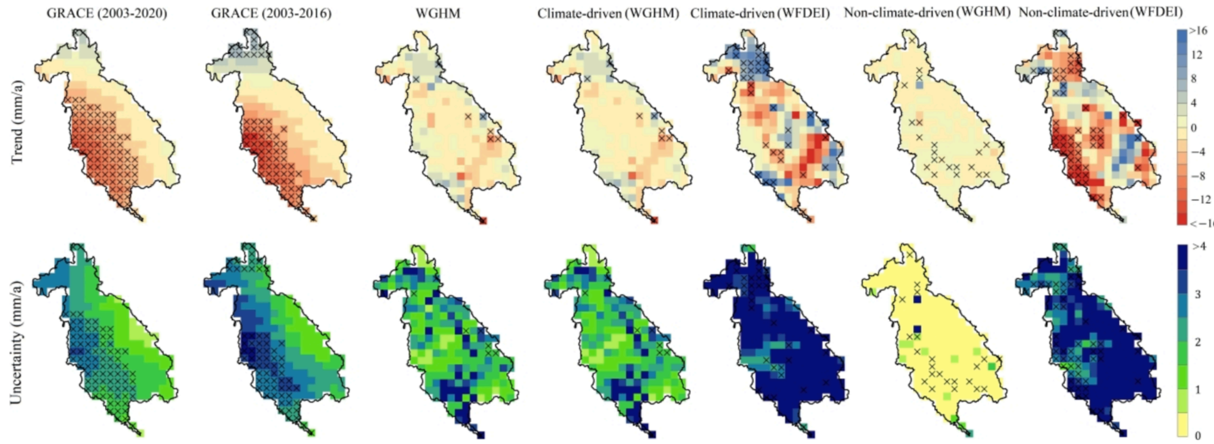

Fig. 3. Spatial distribution of trends (upper panel) and uncertainties (lower panel) in TWSA, climate-driven TWSA, and non-climate-driven from the GRACE, WGHM, and statistical model in the lower MRB during 2003–2020. The black cross indicates the grid cells with significant trends ($p < 0.05$).

distribution of GRACE data is demonstrated for the period 2003–2016, while with relatively higher trends and uncertainties over the basin. WGHM-modeled TWSA generally shares a similar pattern with GRACE data between 2003 and 2016, with increasing trends in the north while decreasing trends mainly in the central and south basin. However, the southwestern, eastern, and southeastern regions illustrate positive trends with trends below 8 mm/a, with uncertainties higher than 3 mm/a. Such differences might arise from the inherent uncertainty of the WGHM and the bias of the climate inputs (i.e., WFDEI dataset). Moreover, the climate-driven TWSA shares similar patterns in both trends and uncertainties with TWSA from 2003 to 2016, implying the governing role of the climatic factors in TWSA variations spatially. The paradigm can be further validated according to the comparable distributions between WGHM outputs and WFDEI-derived climatic reconstructions. In contrast to that, slightly increasing trends of TWSA are captured by the non-climate-driven TWSA in the west and south of the central basin, whose trends are generally below 4.0 mm/a and the uncertainties are lower than 1 mm/a. Forced with the WFDEI climate forcing (same as the WGHM), the non-climate-driven TWSA based on the statistical method illustrates generally similar distribution but with higher amplitudes and uncertainties due to the propagated uncertainty in the identification and separation of the climate-driven parts. We note considerable differences between the climatic and non-climatic TWSA reconstructions exist due to different meteorological forcings (Figs. S7 and S8). However, demonstrative insights can be provided by combining with the WGHM and statistical approach forced by the same dataset (i.e., WDFEI).

Apart from long-term trends, seasonal characteristics of trends in TWSA are additionally analyzed owing to the divergent climate changes in wet and dry seasons together with the seasonality of non-climate factors (e.g., reservoir operation and irrigation). Fig. 4 shows the annual cycles of trends in TWSA, climate-driven TWSA, and non-climate-driven TWSA. It indicates GRACE data has a unimodal distribution that the negative trends from -8.5 ± 3.6 to -7.9 ± 3.2 mm/a mainly occur in August and September and relatively small trends ranging from -5.5 ± 3 (July) to -1.4 ± 1.7 (February) mm/a happen in other months during 2003–2020. There are no apparent differences detected in GRACE TWSA during 2003–2016 than the period 2003–2020. Compared to the GRACE results, the WGHM model demonstrates underestimated trends with rates ranging from -3.5 ± 2.9 (June) to -0.5 ± 1.3 (April) mm/a. Unlike the long-term trends, the seasonal pattern of WGHM TWSA is dominated by soil moisture, with apparent drying in the wet season (mainly from May to June and August to September) and the wetting trend in the dry season (Fig. S4). The seasonal distributions of trends in climate-driven TWSA are also examined, and consistent patterns between the WGHM and the statistical models are observed, especially with that forced with the WFDEI dataset. The climate-driven TWSA generally presents negative trends in the wet season while positive trends in the dry season, which range from -3.5 ± 2.9 (June) to 3.5 ± 2.1 (December) mm/a with considerable uncertainties. Overall deviations among different subsets of climatic reconstructions might be triggered by their inherent differences. As a consequence, the non-climate-driven component of TWSA from the WGHM is slightly positive from August to December, whereas negative trends are found in other months, particularly from January to May in

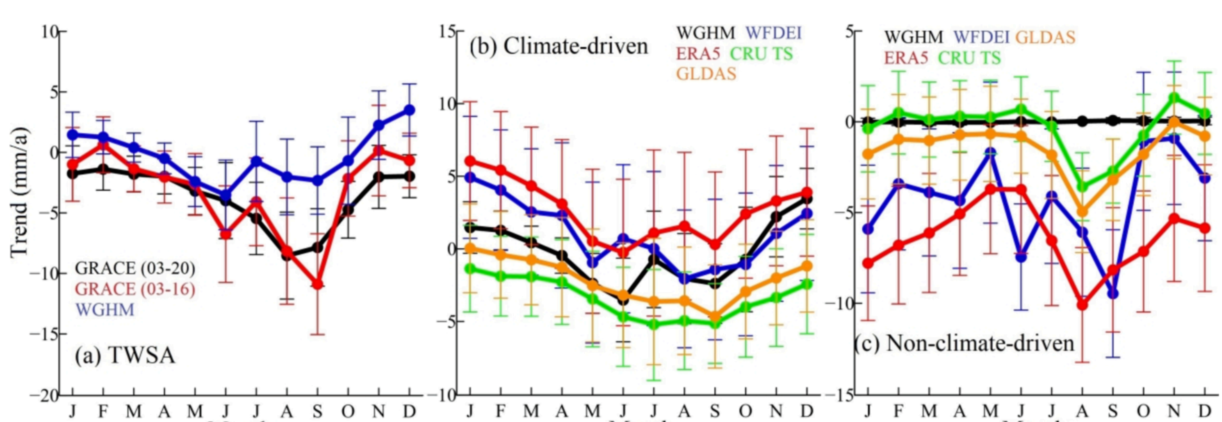

Fig. 4. Annual cycles of trends in (a) TWSA, (b) climate-driven TWSA, and (c) non-climate-driven TWSA from the GRACE, WGHM, and statistical model in the lower MRB during 2003–2020.

the dry season. The differences between the statistically estimated non-climate-driven TWSA and the WGHM simulations can be sourced from the propagated uncertainty of identification, simulation, and/or isolation of the climatic and non-climatic components.

3.2. Influential factors of TWSA

3.2.1. Climatic factors

To assess the influential factors of climate-driven TWSA, multiple climate variables have been analyzed in the lower MRB. Fig. 5 shows the monthly evolution of precipitation and air temperature as well as their trends during 2003–2016. Precipitation generally varies between 1 and 426 mm and shows obvious seasonality due to the monsoon climate. A slight downward trend at a rate of −1.3 ± 8.5 mm/a is detected. Moreover, the air temperature is generally greater than 20.4 ℃ and presents an increasing trend of 0.05 ± 0.02 ℃/a under a warming climate. Consequently, the reducing precipitation and increasing air temperature can reasonably explain the depletion of climate-driven TWSA (−0.3 ± 1.4 mm/a) due to the decreasing water availability under an intensified Earth's water cycle. The annual cycles of trends in different climatic variables are also depicted in Fig. 5. It can be clearly seen that precipitation has a bimodal distribution and there are increasing trends from September to January and June with trends below 3.6 ± 1.6 mm/a (November), while the negative trends with rates from −4.8 ± 2.8 (May) to −0.2 ± 1.8 (April) mm/a appear in the remaining months. In contrast, the air temperature shows a consistent upward trend with trends higher than 0.03 ± 0.01 ℃/a (July) in most of the months except for January (−0.02 ± 0.06 ℃/a) and February (−0.04 ± 0.09 ℃/a). The seasonal distribution of precipitation and air temperature can jointly explain the increase in the climate-driven TWSA from November to January and its decrease in April, May, July, and August. Some disparities in June and March can be attributed to the uncertainty in the trend estimates and the precipitation/air temperature datasets.

The spatial distributions of long-term trends in precipitation and air temperature are presented in Fig. 6. The northern, southeastern, southwestern, and western regions of the basins experience increasing precipitation with trends roughly between 5.0 and 30.0 mm/a, and the uncertainties are correspondingly as high as 30.0 mm/a located in the southwestern area. The central and southern parts witness significant downward trends in precipitation, and the rates change between −30.0 to −15.0 mm/a with the uncertainty between 10.0 and 15.0 mm/a. Comprehensive rising temperature is detected over the lower MRB during 2003–2016, in which the significant trends ($p < 0.05$) are located in the northwestern and southeastern regions. The rates range from 0.01 to 0.11 ℃/a and the uncertainties are favorably low (<0.036 ℃/a), especially in the northwestern region. Generally, the spatial distributions of trends in precipitation and air temperature agree well with those in the climate-driven TWSA including the TWSA gains in the north, centre, and south regions due to precipitation increase and the losses in the northwestern basin from the temperature growth.

3.2.2. Non-climatic factors

Multiple variables including human water use, reservoir regulation, and land cover changes were subject to attribution analysis of non-climate-driven TWSA in the lower MRB. We examined the monthly variations in total water abstraction over the lower MRB during 2003–2016 (Fig. 7), which generally fluctuates between 0 and 6 mm with high inter- and intra-annual variability. An increasing trend of 0.13 ± 0.14 mm/a is identified between 2003 and 2016, and the value is −0.2 ± 0.3 mm/a for the period 2003–2010. However, the sectoral water withdrawals show a different positive trend of 0.2 ± 0.03 mm/a, which might be due to the uncertainty in the WGHM model. Differences between total water abstraction indicate that the summed water withdrawals might arise from the underestimated sectoral water use such as reservoir impoundment in the wet season. Furthermore, the individual sectoral water withdrawal presents the dominating role of irrigation to other categories of human activities such as manufacturing, mining, and electricity (Fig. S9), and it also has the highest increasing trend of 0.08 ± 0.03 mm/a during 2003–2010. In addition, seasonal distribution in water abstraction shows slight positive trends from February to March, from May to August, and December, which might cause the decrease in non-climate-driven TWSA. However, such effects might be constrained due to relatively small amplitudes (<0.08 ± 0.05 mm/a). The spatial distribution of trends in total water abstraction during 2003–2016 suggests the regions with significant increasing values are mainly located in the southeast of the basin (Fig. 8), which might be caused by the rapid urbanization and expansion of the Mekong Delta (Yun et al., 2021a). Both increasing and decreasing trends are detected in the west-central basin that is highly irrigated (Fig. S10) due to the changes in irrigations area regionally, with trends ranging from −2.4 ± 1.6 to 1.6 ± 1.5 mm/a. We also examined the annual irrigation map over the lower MRB from 2001 to 2015, indicating both an increase and decrease in irrigation area over the centre basin, agreeing with the spatial changes in water extraction (Fig. 9). Specifically, the percentage of grid cells with high irrigation shows a downward trend of −0.05 ± 0.01 %/a, while an upward trend of 0.03 ± 0.16 %/a is found for the area with low to medium irrigation between 2001 and 2015. The annual irrigation maps are depicted to show the spatiotemporal variations of irrigation area over the lower MRB (Fig. S11).

The reservoir storage generally changes between 3.9 ± 0.4 and 16.6 ± 1.7 mm and shows a non-significant increasing trend (0.01 ± 0.08 mm/a) during the period 2003–2016 (Fig. 7), favouring the increase of non-climate-driven TWSA. Annual cycles of trends do not present a significant trend from January to September except for May (0.02 ± 0.06 mm/a) but steadily grow from October (0.02 ± 0.22 mm/a) to December (0.08 ± 0.2 mm/a). The changing pattern of reservoir storage can partly explain the seasonal distribution of trends in non-climate-

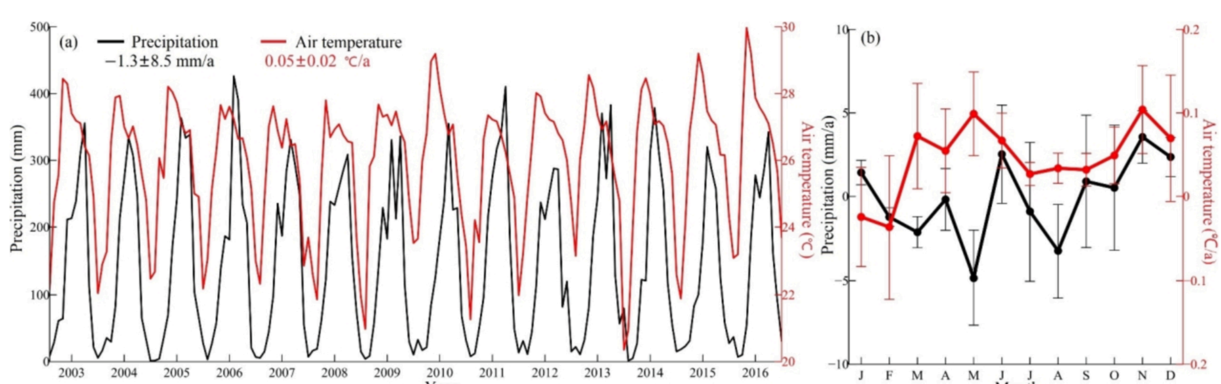

Fig. 5. (a) Monthly time series and (b) annual cycle of trends in precipitation and air temperature from the WFDEI dataset in the lower MRB during 2003–2016.

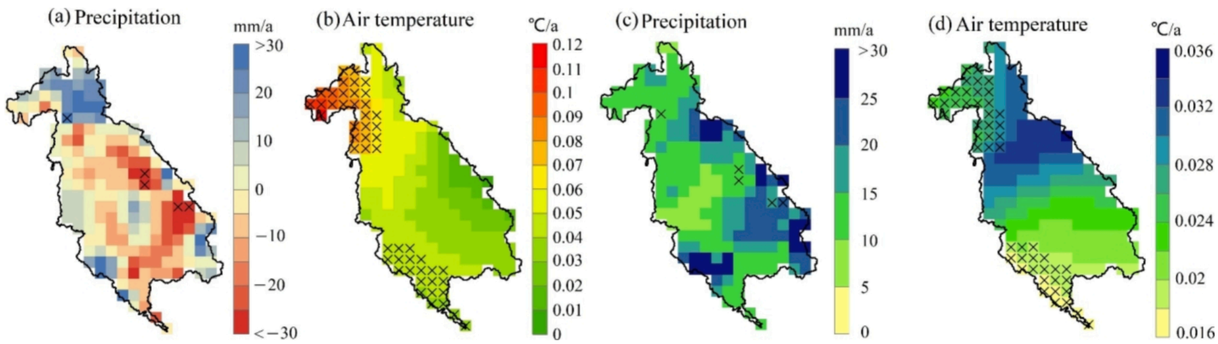

Fig. 6. Spatial distribution of (a, b) trends and (c, d) uncertainties in precipitation and air temperature in the lower MRB during 2003–2016. The black cross indicates the grid cells with significant trends ($p < 0.05$).

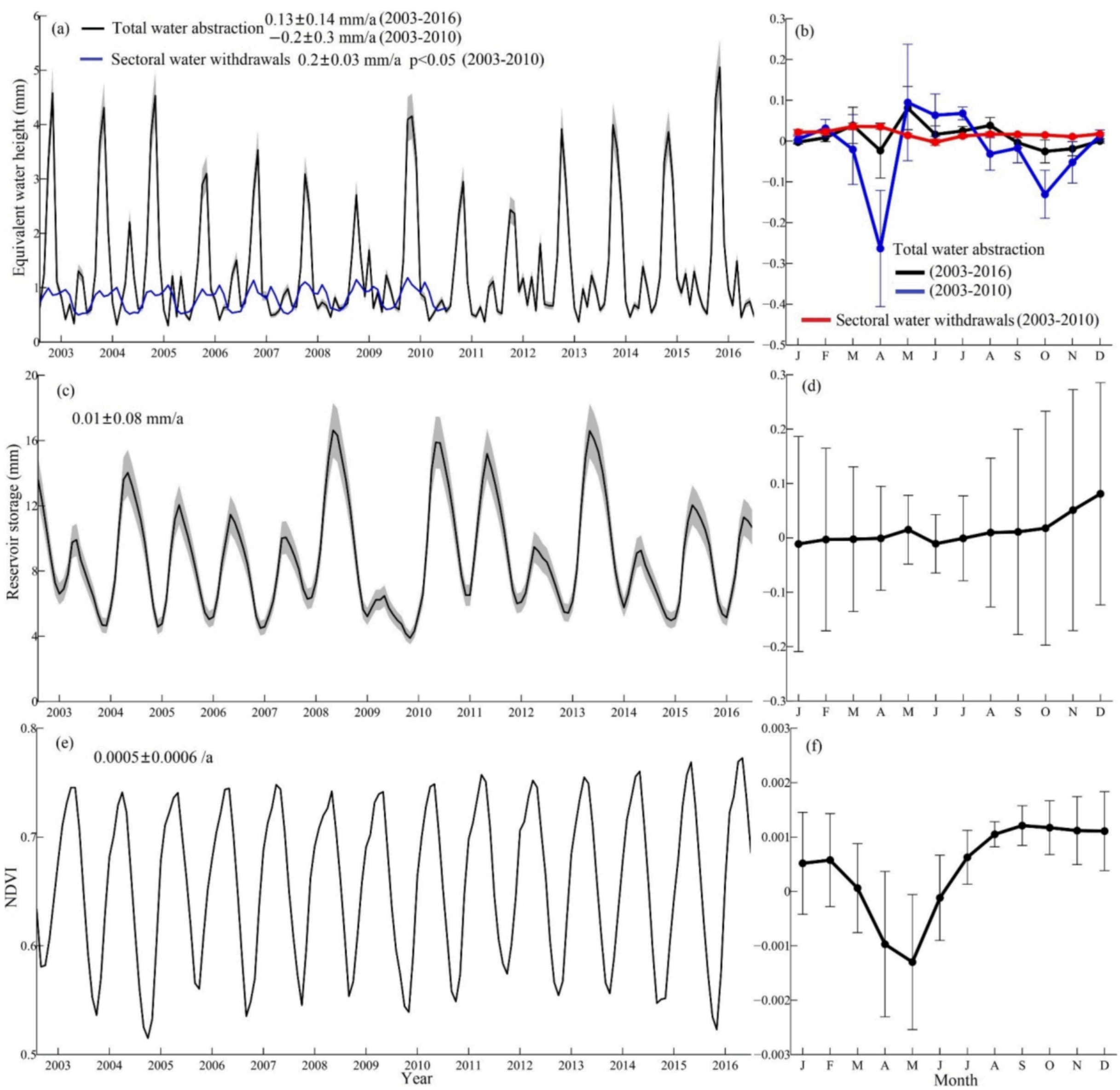

Fig. 7. Monthly time series (left panel) and annual cycle in trends (right panel) of (a, b) total water abstraction, (c, d) reservoir storage, and (e, f) NDVI in the lower MRB during 2003–2016.

driven TWSA as well as its positive trend on the yearly scale, even though the magnitude is relatively low (0.01 ± 0.07 mm/a). There are no significant changes in reservoir storage that can be observed for the whole of lower MRB, with only a few reservoirs in the lower reach experiencing surface water depletion. The uncertainty of trends is relatively high in the west compared to that in the south of the basin.

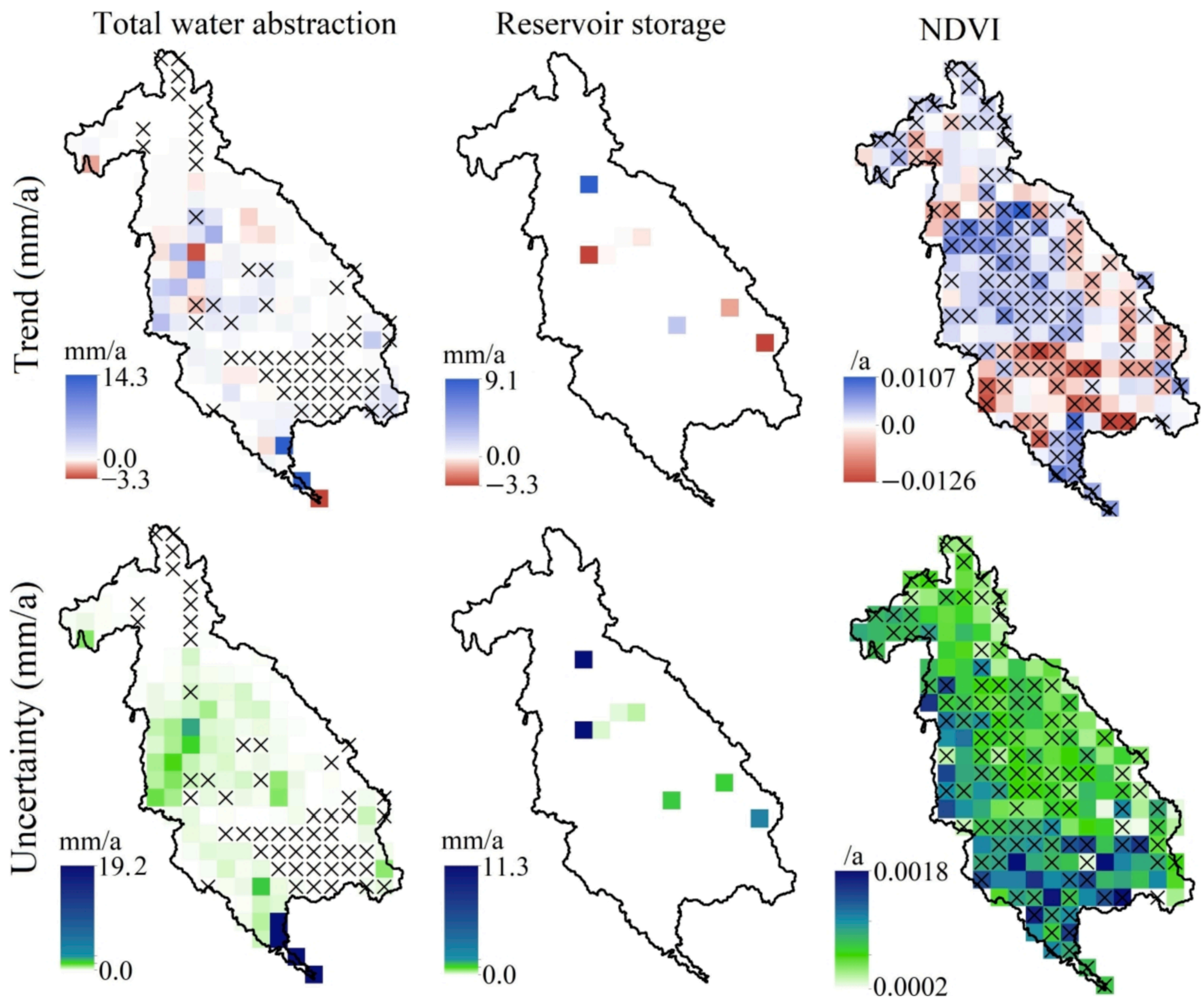

Fig. 8. Spatial distribution of trends (upper panel) and uncertainties (right panel) in NDVI, net abstraction, and reservoir storage in the lower MRB during 2003–2020. The black cross indicates the grid cells with significant trends ($p < 0.05$).

Such distribution and amplitude demonstrate similar patterns of the non-climate-driven TWSA suggest the potential impacts of reservoir constructions on the regional non-climatic TWSA variations.

Human activities such as dam operation and agricultural expansion can generally be considered as the main factors deriving the land use/land cover changes in the lower MRB (Cho and Qi, 2021). No apparent trend in NDVI is determined (0.0005 ± 0.0006 /a), while the decreasing trends between April (0.001 ± 0.0013 /a) and June (0.0001 ± 0.0009 /a) combined with the increasing trends from July (0.0006 ± 0.0005 /a) to March (0 ± 0.0008 /a) are identified. Such distribution could reflect the effects of various human activities on the regional land cover such as irrigation and urbanization. Spatially, NDVI illustrates significant downward trends in the south of lower MRB, which may be due to the rapid urbanization process over the Mekong Delta (Yun et al., 2021a). Differently, some areas in the central basin have growing NDVI, consistent with the changes in the irrigation area. These patterns are also validated by the annual map of land cover during 2003–2020 (Fig. S12).

3.3. Future projections of TWSA

Given the considerable differences among climatic projections from different GCMs (i.e., GFDL-ESM2M, HADGEM2-ES, IPSL-CM5A-LR, MIROC5), we used the GTCH method to evaluate the individual uncertainty and fuse the WGHM-based TWSA projections under multiple scenarios (i.e., RCP2.6, RCP6.0, and RCP8.5). Table S4 summarizes the basin-scale results, indicating the GFDL-ESM2M model has the highest uncertainty under different scenarios while the IPSL-CM5A-LR output shows the lowest except for the RCP2.6 scenario (MIROC5). Consequently, the relatively high weights were assigned to the IPSL-CM5A-LR and MIROC5 models, while low weight was given to the GFDL-ESM2M data. Spatially, similar distributions of uncertainties are observed on the grid scale under multiple scenarios, in which there are higher values along with the Mekong River stretch (Figs. S13 and S14). The IPSL-CM5A-LR and MIROC5 models also show comparatively low uncertainties than the GFDL-ESM2M and HADGEM2-ES data, which generally translate to higher weights for the fused TWSA projections forced with different GCMs. Hence, we developed the fused WGHM-projected TWSA forced with four GCMs at both grid and basin scales to alleviate the forcing uncertainty. Similarly, the precipitation and air temperature are also fused to analyze the future climatic variabilities over the lower MRB.

Fig. 10 exhibits the projected changes in TWSA driven by projected climate changes in the lower MRB during the period 2030–2099. Projected TWSA changes under RCP8.5 scenario are smaller than the RCP2.6 and RCP6.0 results with relatively high uncertainties sourced from various climate forcings, especially during the extreme wet and dry periods. No obvious differences between the RCP2.6 and RCP6.0 scenarios are observed except for the peaks and troughs. Generally, an increasing trend of 0.16 ± 0.11 mm/a during 2030–2099 is calculated under the RCP2.6 scenario, and the value changes to 0.1 ± 0.12 mm/a for the RCP6.0 scenario. However, a negative trend of −0.06 ± 0.11 mm/a is estimated for the RCP8.5 scenario. In addition, we identified

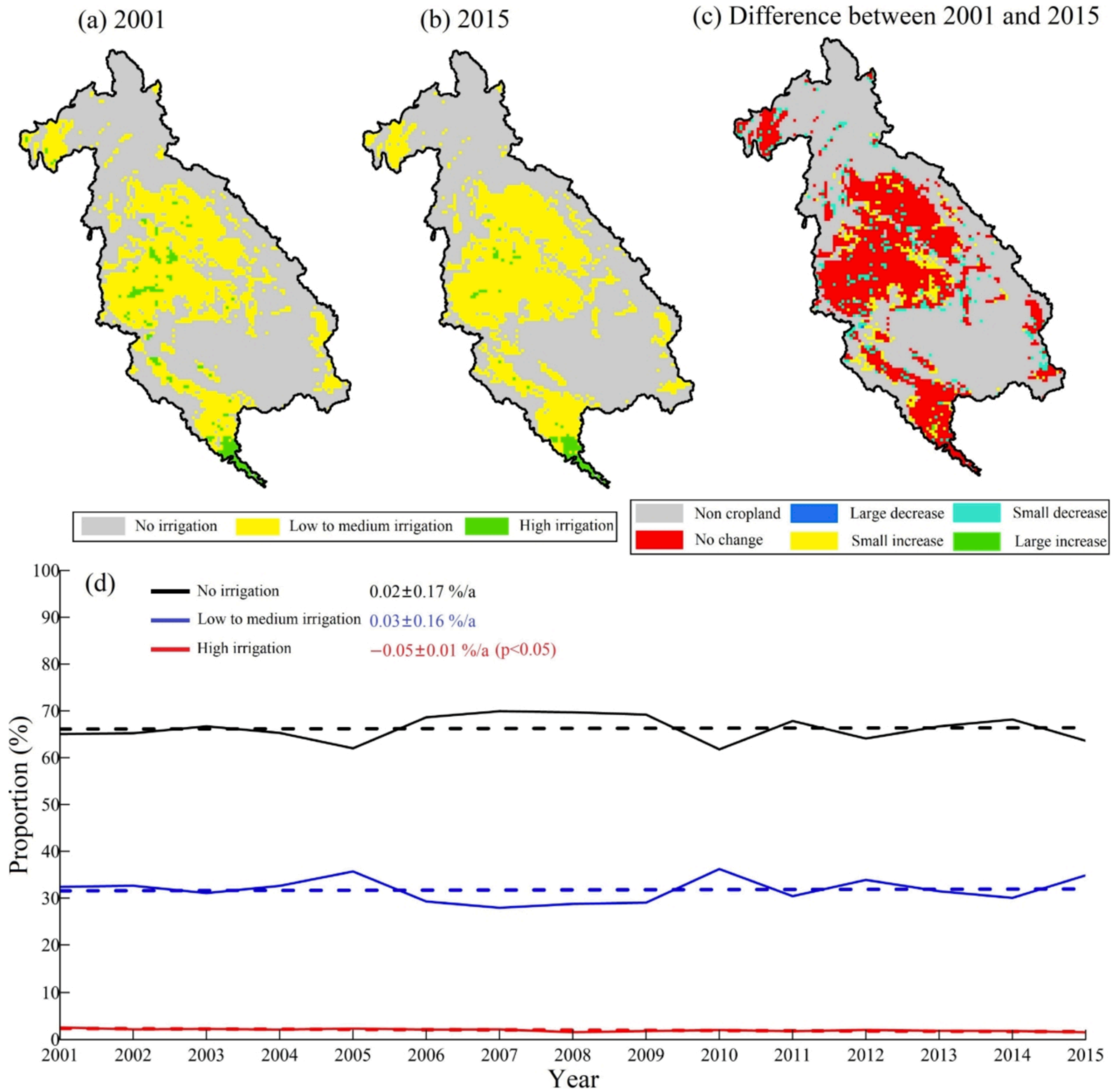

Fig. 9. Spatial distribution of irrigation maps in (a) 2001, (b) 2015, and (c) changes from 2001 to 2015. Subplot (d) indicates inter-annual changes in the percentage of grid cells with no irrigation, low to medium irrigation, and high irrigation area over the lower MRB from 2001 to 2015.

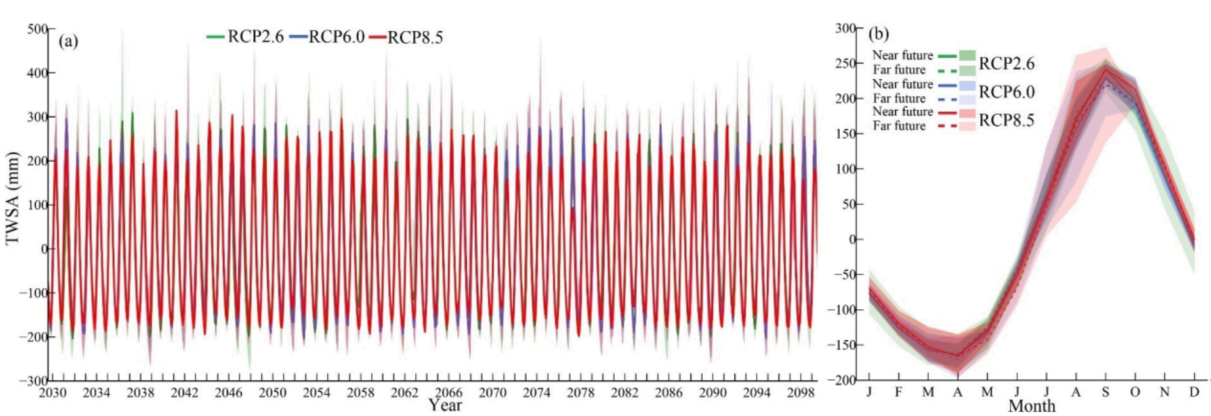

Fig. 10. (a) Temporal changes and (b) annual cycles of projected TWSA in the lower MRB during the period 2030–2099 under RCP2.6, RCP6.0, and RCP8.5 scenarios. The near future and far future indicates the period 2040–2059 and 2080–2099, respectively. The shade represents the change range of WGHM simulations forced with different GCMs.

the annual cycle of projected TWSA in the near (2040–2059) and far (2080–2099) future periods (Fig. 10). Similar distributions are discovered under multiple scenarios and periods, suggesting TWSA increases from April to September and decreases from October to March. In the near future, the projected TWSA under RCP8.5 scenario shows high values compared with the RCP2.6 and RCP6.0 scenarios, particularly in the wet season. However, the relatively lower TWSA is projected for the RCP8.5 scenario in the far future. Moreover, the uncertainties in projected TWSA are larger in the extremely dry/wet months than in other months, and the differences become more obvious during the far future than in the near future. Higher inter-model variabilities are observed among different GCMs under the RCP8.5 scenarios than the other two scenarios. In addition to the fused TWSA, the ensemble mean of various simulations forced by the four GCMs is also presented (Fig. S15).

The spatial distribution of absolute changes in future TWSA over the lower MRB is illustrated (Fig. 11). Under the RCP2.6 scenario, TWSA increases roughly ranging from 10 to 50 mm are discovered along the Mekong River and in the northwestern and southwestern of the basin in the near future, with the uncertainties generally greater than 10 mm (Fig. S16). Despite the subsequent enhancement of TWSA over the lower reach, some TWSA reduction below −10 mm is found over the eastern region in the far future with overall higher uncertainties than the near future. The RCP6.0 results present a similar pattern to the RCP2.6 scenario except for some TWSA loss in the southwestern region in the near future, which spread to the surrounding area in the far future. However, the TWSA gains in the northwestern basin alleviate under the RCP8.5 scenario with the decreased TWSA in the east basin. Furthermore, the majority of the region in the central and northern basins experiences a TWSA deficit in the far future. The basin-averaged examinations indicate that TWSA is projected to increase by 12.2 ± 12.2 mm and 11.6 ± 25.8 mm under the RCP2.6 scenario in the near and far future, respectively. The numbers are similar to the RCP6.0 scenario, that is, 10.3 ± 18.9 mm (near future) and 12.3 ± 30 mm (far future). However, the RCP8.5 scenario project a lower TWSA increase of 9.3 ± 21.4 mm and 1.6 ± 41.2 mm for the near and far future periods, respectively. The projected patterns of TWSA are closely associated with the projected future changes in precipitation and air temperature both temporally and spatially (Figs. S17 and S18). For example, the overall increase in precipitation in the northwest and south of the basin contributes to the TWSA increase under the RCP8.5 scenario, especially for the lower reach of the Mekong River. While the eastern basin is projected to undergo severe precipitation decrease as low as ~ −40 mm, in agreement with the TWSA distributions. Such patterns can be intensified under the sharply increasing air temperature, which reaches 4℃ in the upper reach of the lower MRB.

To examine the future variations of flood potential with changing precipitation and TWSA, we compared the probability density distributions of FPI during the past (2003–2020) and future (i.e., near (2040–2059) and far (2080–2099) future) periods (Fig. 12). The overall positive offsets can be observed among historical and future periods under different climate change scenarios, highlighting increased flood potential over the lower MRB in the 21st century due to increased precipitation, which is more obvious for the high-flood-risk periods. Specifically, the durations with relatively high flood potential (FPI greater than 0.5) have increased by 3.5 ± 2.2 % in both the near and far future compared to the past period under the RCP2.6 scenario (Fig. 12). The percentages reach 3.0 ± 1.9 % and 8.8 ± 1.1 % during the near future for the RCP6.0 and RCP8.5 scenarios, respectively. They are projected to be 4.3 ± 3.8 % (RCP6.0) and 4.6 ± 2.7 % (RCP8.5) in the far future. In a nutshell, the increasing flood potential induced by the changes in TWSA and precipitation can be identified under multiple scenarios in both the near and far future.

4. Discussion

A few studies have assessed the historical and future changes of TWSA in the lower MRB. Jing et al. (2020) used five different GRACE mascon and spherical harmonics solutions to detect the TWSA trends in the lower MRB, and an insignificant negative tendency was discovered based on Mann-Kendall test and time series decomposition methods during the period 2003–2016. On the contrary, the current study obtained a negative trend of −3.3 ± 2.2 and −0.3 ± 1.4 mm/a between

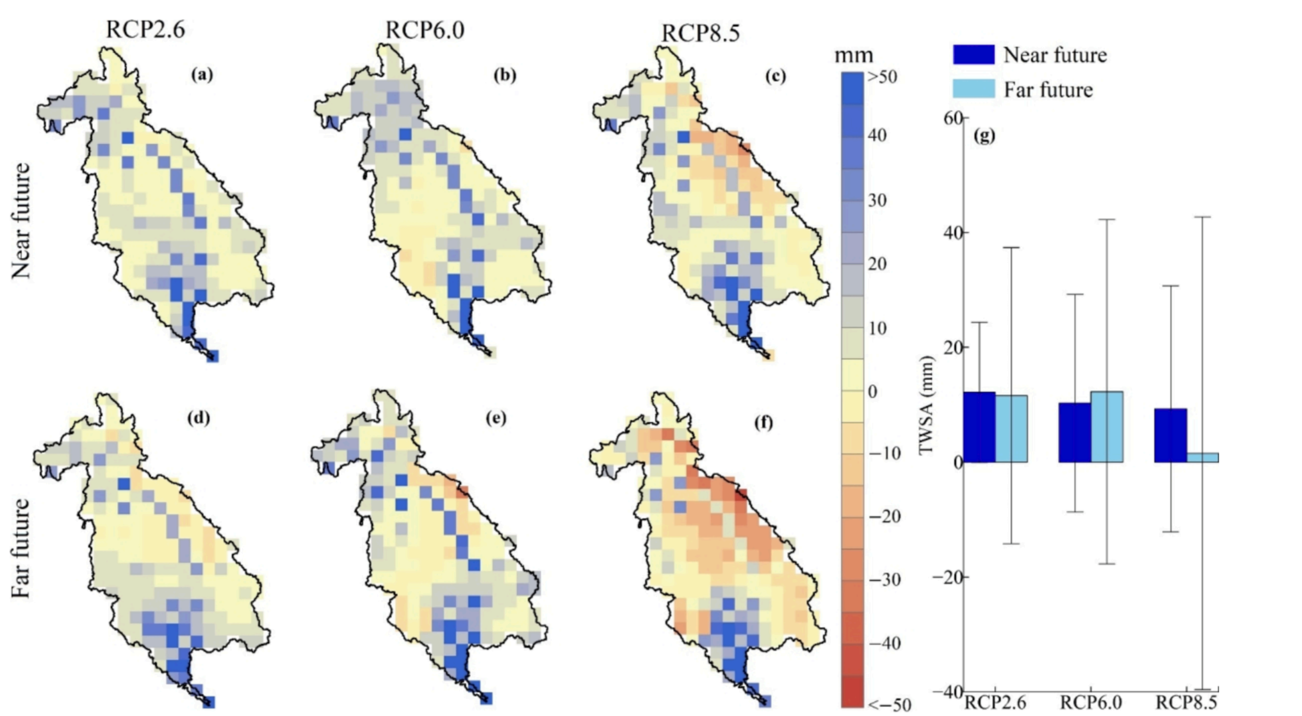

Fig. 11. (a-f) Spatial distribution and (g) basin-averaged value of projected TWSA changes over the lower MRB during the near (2040–2059) and far (2080–2099) future relative to the past period (2003–2020) under RCP2.6, RCP6.0, and RCP8.5 scenarios. The uncertainty is taken as the standard deviation of WGHM simulations forced with different GCMs.

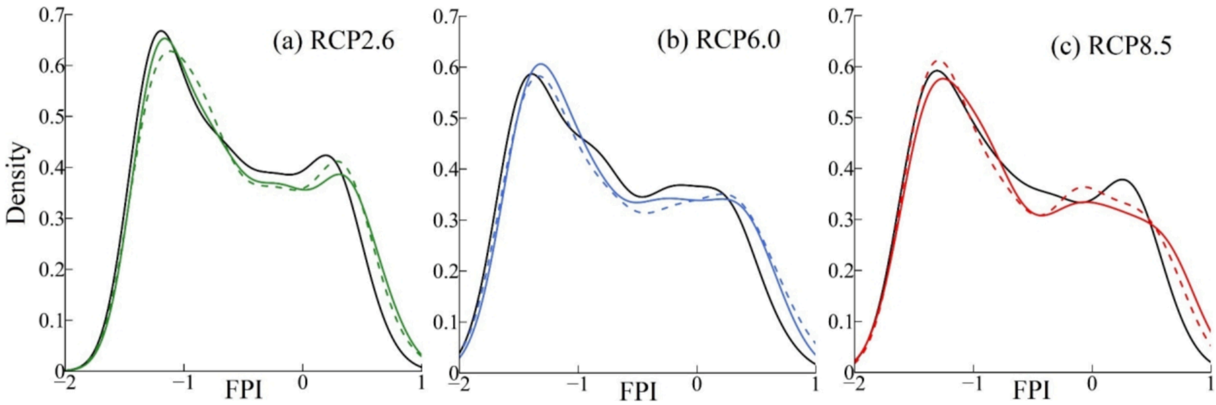

Fig. 12. Probability density functions of FPI in the lower MRB during the past period (2003–2020), near future (2040–2059), and far future (2080–2099) under (a) RCP2.6, (b) RCP6.0, and (c) RCP8.5 scenarios. The black indicates the historical results. The coloured solid and dash lines represent the near and far future results, respectively.

2003 and 2016 using the linear regression approach based on the reconstructed CSR mascon solution and WGHM model, respectively. The slight difference can be triggered by the uncertainty in the different data used and distinctive calculation methods. Nevertheless, another global perspective revealed a decreasing trend of TWSA during the period 2002–2016 over the majority of the MRB, especially in the midstream and downstream reaches (Rodell et al., 2018), which is in line with our findings. A recent study attempted to track the long-term trends in TWSA around the upper reach of the MRB, and also found significant negative trends ranging from −3.2 to −6.0 mm/a, close to the results of this study for the lower basin (Bibi et al., 2021). However, these studies merely focused on the changes in full TWSA, neglecting the respective non-climate-driven and climate-driven parts of TWSA, particularly in the context of significant human activity (Fig. S19) and climate change over the last decades (Liu et al., 2021). In terms of future changes in TWSA, Pokhrel (2021) utilized seven different LSMs, GHMs, and DGVM forced with four GCMs from the CMIP5 archive to assess the future projections of global TWSA under RCP2.6 and RCP6.0 scenarios. It was found that the TWSA over the southeastern of the lower MRB was projected to increase while the other regions presented a decrease, under RCP2.6 and RCP6.0 scenarios in the late century (2070–2099) compared with the historical baseline from 1976 to 2005, which are generally in line with our results despite different calculation periods and models. By combing the GCMs and hydrological model, the increased flood potential was reported by previous research (Wang et al., 2021; Yun et al., 2021a), coinciding with the enhancement of flood potential in our study.

To sum up, this study systematically investigated the non-climate-driven and climate-driven TWSA in the past (2003–2020) and future projections of TWSA (2030–2099), improving the understanding of the hydrological response to global change (Greve et al., 2014). Given the increasingly frequent water conflicts within different countries, partitioning the climate-driven and non-climate-driven components of TWSA is essential for better management and cooperation of water-related resources (Fan and He, 2015; Yun et al., 2021b). Assessing the divergent changes in the two components of TWSA also provides important implications for water balance studies in other basins worldwide with rapid reservoir constructions and varying climate conditions (e.g., precipitation and evapotranspiration) (Famiglietti and Rodell, 2013; Chao et al., 2020). Moreover, projecting future TWSA under multiple scenarios indeed can be dedicated to the exploration of terrestrial dryness/wetness and associated changes in hydrological extremes like floods and droughts in the future (Xiong et al., 2022).

Although the historical and future TWSA changes under the background of climatic and non-climatic changes have been successfully characterized, there are still some limitations existing at the current stage. Despite the use of reconstructed GRACE-like products, the relatively short time and a total of 33 missing months of GRACE satellites (∼21 years) could inevitably generate the uncertainty for continuous monitoring of the TWSA variability at the climate scale (i.e., greater than30 years) (Ghobadi-Far et al., 2020; Sun et al., 2020), thus challenging the reasonable and accurate estimates of long-term trends in TWSA, especially for the lower MRB that has undergone significant climate changes and human activities over decades (Nie et al., 2018). The human water use and reservoir operation data are derived from the WGHM owing to the restricted data-sharing policies among different countries, whose outputs are only available until the end of 2016, causing the inconsistency with the study period (2003–2020) of our research. This difference might impact the rationality of the attribution analysis of non-climate-driven TWSA. Also, the future projections used in this study, developed under the framework of ISI-MIP 2b phase, were forced by the GCM outputs from the CMIP5 archive. Although the meteorological forcing data has gone through a bias-correction and downscaling, their bias may be higher than the latest CMIP6 GCM data (Eyring et al., 2016; Ferguson et al., 2018). The simulation round for the future scenario (2006–2099) is also relatively longer than that of the CMIP6 archive (2015–2099), resulting in higher uncertainty in TWSA simulations in this study. Hence the social-economic conditions have been fixed at the 2005 level during the future projection, which might have underestimated the influences of human activities such as reservoir regulation because of the rapid reservoir constructions after the year (Yun et al., 2021a).

5. Conclusions

In this study, we identified the recent changes of TWSA in the lower MRB during 2003–2020, and partitioned it into the climate-driven and non-climate-driven TWSA during the period 2003–2016 based on the WGHM model and a statistical approach. Subsequently, the spatiotemporal variability of the full TWSA and its two components have been investigated. Furthermore, the attribution analysis was performed in combination with multiple climatic (i.e., precipitation and air temperature) and non-climatic (i.e., water abstraction, reservoir storage, and land cover) factors. Moreover, the future projections of TWSA under RCP2.6, RCP6.0, and RCP8.5 scenarios have been conducted for the period 2030–2099 using the WGHM model forced with four downscaled and bias-corrected simulations of four CMIP5 GCMs, which were subsequently integrated using the GTCH method to eliminate the inter-model uncertainties. Two future periods (i.e., near (2040–2059) and far (2080–2099) future) are analyzed independently. In addition, the future changes in flood potential that closely relate to precipitation and TWSA were also analyzed. The main findings and conclusions are summarized as follows:

(1) GRACE TWSA decreases at a rate of −3.3 ± 2.2 mm/a (−3.7 ± 1.8 mm/a) that mainly occurs in the months from July to October during 2003–2016 (2003–2020), and the trend is −0.3 ± 1.4 mm/a based on the WGHM outputs. Climate-driven TWSA derived from the WGHM model and statistical method forced with different datasets are highly correlated with the correlation coefficients ranging from 0.81 to 0.91. It exhibits a similarly negative trend (−0.3 ± 1.4 mm/a) and the seasonal distribution to the full TWSA, while the non-climate-driven part presents a small positive trend (0.01 ± 0.07 mm/a) that occurs during August-December. Spatially, the GRACE TWSA shows an apparent pattern with a depletion in the southwestern region and an increase in the northern region during 2003–2016 (2020), which is consistent with spatial pattern of the changes in the climatic components. However, the non-climate-driven TWSA component presents a slight increase over the west and south of the central basin. Consequently, the trend in full TWSA is dominated by climatic factors, while the influence of the non-climatic factors is limited.

(2) Decreasing trends of precipitation (−1.3 ± 8.5 mm/a) and rising air temperature (0.05 ± 0.02 ℃/a) are detected during 2003–2016. The annual cycle and spatial distribution of precipitation are consistent with the climate-driven TWSA, with the comprehensive warming climate over the lower MRB. The variations in precipitation and air temperature can well explain the patterns of the climatic TWSA. A slight enhancement in human water abstraction (0.13 ± 0.14 mm/a during 2003–2020) and sectoral water withdrawal (e.g., irrigation) (0.2 ± 0.03 mm/a during 2003–2010) that are mainly located in the south and west-central regions are identified, causing regional depletion in non-climate-driven TWSA. The increase in reservoir storage (0.01 ± 0.08 mm/a) is considered responsible for the growth of non-climate-driven TWSA, which can also be reflected by their consistent seasonal characteristics and spatial distribution. Changes in land cover from the varying NDVI can further support our attributions for non-climate-driven TWSA, including the decreasing trends over the southern basin due to urbanization and increasing trends over the central region because of the irrigation area changes.

(3) The GTCH method explicitly quantifies the uncertainty of TWSA projections forced by different GCMs, and their respective weights are estimated for data fusion. Under the RCP2.6 scenario, TWSA is expected to increase at a rate of 0.16 ± 0.11 mm/a during 2030–2099, and the trend changes to 0.1 ± 0.12 and −0.06 ± 0.11 mm/a for the RCP6.0 and RCP8.5 scenarios, respectively. TWSA is projected to increase by 12.2 ± 12.2 mm and 11.6 ± 25.8 mm under the RCP2.6 scenario in the near and far future, respectively. The increase is similar for the RCP6.0 scenario (i.e., 10.3 ± 18.9 mm in the near and 12.3 ± 30 mm in the far future). However, the RCP8.5 scenario projects a lower TWSA increase of 9.3 ± 21.4 mm and 1.6 ± 41.2 mm for the near and far future periods, respectively. The projected changes of TWSA can be well explained by the future changes in precipitation and air temperature temporally and spatially. An increase in flood potential induced by the changes in TWSA and precipitation is identified under multiple scenarios in both the near and far future.

Our results may foster the urgent discussion on a shift of the water withdrawals and allocations from the supply side (e.g., over-abstraction) to the demand side (e.g., using less water intense crops, revising pumping regulations, upgrading the prevailing irrigation and water supply technology to minimize the losses). The results are expected to call attention to value-added multilateral cooperation among the various nations and stakeholders to incentivize the water-sharing agreements to mitigate the future potential issues in the vicinity of the Mekong river basin.

Data Availability

All the data and models generated or used during the study appear in the submitted article or in the supplementary file.

CRediT authorship contribution statement

Jinghua Xiong: Conceptualization, Visualization, Data curation, Writing – original draft. **Shenglian Guo:** Writing – review & editing, Supervision, Funding acquisition, Project administration. **Deliang Chen:** Conceptualization, Visualization, Data curation, Writing – original draft. **Yulong Zhong:** Conceptualization, Visualization, Data curation, Writing – original draft. **Bingshi Liu:** Conceptualization, Visualization, Data curation, Writing – original draft. **Abhishek:** Conceptualization, Visualization, Data curation, Writing – original draft. **Jiabo Yin:** Writing – review & editing.

Declaration of Competing Interest

The authors declare that they have no known competing financial interests or personal relationships that could have appeared to influence the work reported in this paper.

Data availability

Data will be made available on request.

Acknowledgments

This study was financially supported by the National Key Research and Development Program of China (2021YFC3200303), the Strategic Priority Research Program of the Chinese Academy of Sciences (XDA20060402), and the Swedish STINT (CH2019-8377 and CH2020-8767). The numerical calculations in this paper have been done on the supercomputing system in the Supercomputing Center of Wuhan University. The authors thank Linli An for helping acquire the WGHM outputs under the "nosoc" scenario.

Appendix A. Supplementary data

Supplementary data to this article can be found online at https://doi.org/10.1016/j.jhydrol.2022.128275.

References

Abhishek, Kinouchi, T., 2022. Multidecadal Land Water and Groundwater Drought Evaluation in Peninsular India. Remote Sen. 14, 1486.

Abhishek, Kinouchi, T., Sayama, T., 2021. A comprehensive assessment of water storage dynamics and hydroclimatic extremes in the Chao Phraya River Basin during 2002–2020. J. Hydrol. 603, 126868. https://doi.org/10.1016/j.jhydrol.2021.126868.

An, L., Wang, J., Huang, J., Pokhrel, Y., Hugonnet, R., Wada, Y., Cáceres, D., Müller Schmied, H., Song, C., Berthier, E., Yu, H., Zhang, G. 2021. Divergent causes of terrestrial water storage decline between drylands and humid regions globally. Geophysical Research Letters, 48(23), e2021GL095035.

Bibi, S., Song, Q., Zhang, Y., Liu, Y., Kamran, M.A., Sha, L., Zhou, W., Wang, S., Gnanamoorthy, P., 2021. Effects of climate change on terrestrial water storage and basin discharge in the lancang River Basin. J. Hydrol. Reg. Stud. 37, 100896 https://doi.org/10.1016/j.ejrh.2021.100896.

Campbell, I.C., Say, S., Beardall, J., 2009. Tonle Sap Lake, the heart of the lower Mekong. The Mekong. Elsevier 251–272.

Chao, N., Chen, G., Wang, Z., 2020. Impact of Eastern Tibetan Plateau Glacier Melt on Land Water Storage Change across the Yangtze River Basin. J. Hydrol. Eng. 25, 05020002. https://doi.org/10.1061/(ASCE)HE.1943-5584.0001882.

Chen, A., Liu, J., Kummu, M., Varis, O., Tang, Q., Mao, G., Wang, J., Chen, D., 2021. Multidecadal variability of the Tonle Sap Lake flood pulse regime. Hydrol. Process. 35 (9) https://doi.org/10.1002/hyp.14327.

Cho, N., Qi, J., 2021. Quantifying spatiotemporal impacts of hydro-dams on land use/land cover changes in the Lower Mekong River Basin. Applied Geography 136, 102588. https://doi.org/10.1016/j.apgeog.2021.102588.

Eicker, A., Schumacher, M., Kusche, J., Döll, P., Schmied, H.M., 2014. Calibration/Data Assimilation Approach for Integrating GRACE Data into the WaterGAP Global Hydrology Model (WGHM) Using an Ensemble Kalman Filter: First Results. Surv. Geophys. 35, 1285–1309. https://doi.org/10.1007/s10712-014-9309-8.

Eicker, A., Forootan, E., Springer, A., Longuevergne, L., Kusche, J., 2016. Does GRACE see the terrestrial water cycle "intensifying"?: WATER CYCLE INTENSIFICATION WITH GRACE. J. Geophys. Res. Atmospheres 121, 733–745. https://doi.org/10.1002/2015JD023808.

ESA. Land Cover CCI Product User Guide Version 2. Tech. Rep. (2017). Available at: maps.elie.ucl.ac.be/CCI/viewer/download/ESACCI-LC-Ph2-PUGv2_2.0.pdf.

Eyring, V., Bony, S., Meehl, G.A., Senior, C.A., Stevens, B., Stouffer, R.J., Taylor, K.E., 2016. Overview of the Coupled Model Intercomparison Project Phase 6 (CMIP6) experimental design and organization. Geosci. Model Dev. 9, 1937–1958. https://doi.org/10.5194/gmd-9-1937-2016.

Famiglietti, J.S., Rodell, M., 2013. Water in the Balance. Science 340, 1300–1301. https://doi.org/10.1126/science.1236460.

Fan, H., He, D., 2015. Temperature and Precipitation Variability and Its Effects on Streamflow in the Upstream Regions of the Lancang-Mekong and Nu–Salween Rivers. J. Hydrometeorol. 16, 2248–2263. https://doi.org/10.1175/JHM-D-14-0238.1.

Ferguson, C.R., Pan, M., Oki, T., 2018. The Effect of Global Warming on Future Water Availability: CMIP5 Synthesis. Water Resour. Res. 54, 7791–7819. https://doi.org/10.1029/2018WR022792.

Gao, J., Yao, T., Masson-Delmotte, V., Steen-Larsen, H.C., Wang, W., 2019. Collapsing glaciers threaten Asia's water supplies. Nature 565, 19–21. https://doi.org/10.1038/d41586-018-07838-4.

Ghobadi-Far, K., Han, S.-C., McCullough, C.M., Wiese, D.N., Yuan, D.-N., Landerer, F.W., Sauber, J., Watkins, M.M., 2020. GRACE Follow-On Laser Ranging Interferometer Measurements Uniquely Distinguish Short-Wavelength Gravitational Perturbations. Geophys. Res. Lett. 47, e2020GL089445. https://doi.org/10.1029/2020GL089445.

Greve, P., Orlowsky, B., Mueller, B., Sheffield, J., Reichstein, M., Seneviratne, S.I., 2014. Global assessment of trends in wetting and drying over land. Nat. Geosci. 7 (10), 716–721.

Guo, L., Li, T., Chen, D., Liu, J., He, B., Zhang, Y., 2021. Links between global terrestrial water storage and large-scale modes of climatic variability. J. Hydrol. 598, 126419.

Hempel, S., Frieler, K., Warszawski, L., Schewe, J., Piontek, F., 2013. A trend-preserving bias correction; the ISI-MIP approach. Earth Syst. Dyn. 4, 219–236. https://doi.org/10.5194/esd-4-219-2013.

Hersbach, H., Bell, B., Berrisford, P., Hirahara, S., Horanyi, A., Munoz-Sabater, J., Nicolas, J., Peubey, C., Radu, R., Schepers, D., Simmons, A., Soci, C., Abdalla, S., Abellan, X., Balsamo, G., Bechtold, P., Biavati, G., Bidlot, J., Bonavita, M., De Chiara, G., Dahlgren, P., Dee, D., Diamantakis, M., Dragani, R., Flemming, J., Forbes, R., Fuentes, M., Geer, A., Haimberger, L., Healy, S., Hogan, R.J., Holm, E., Janiskova, M., Keeley, S., Laloyaux, P., Lopez, P., Lupu, C., Radnoti, G., de Rosnay, P., Rozum, I., Vamborg, F., Villaume, S., Thepaut, J.-N., 2020. The ERA5 global reanalysis. Q. J. R. Meteorol. Soc. 146, 1999–2049. https://doi.org/10.1002/qj.3803.

Hosseini-Moghari, S.-M., Araghinejad, S., Tourian, M.J., Ebrahimi, K., Döll, P., 2020. Quantifying the impacts of human water use and climate variations on recent drying of Lake Urmia basin: the value of different sets of spaceborne and in situ data for calibrating a global hydrological model. Hydrol. Earth Syst. Sci. 24, 1939–1956. https://doi.org/10.5194/hess-24-1939-2020.

Huang, Z., Hejazi, M., Li, X., Tang, Q., Vernon, C., Leng, G., et al., 2018. Reconstruction of global gridded monthly sectoral water withdrawals for 1971–2010 and analysis of their spatiotemporal patterns. Hydrol. Earth System Sci. 22 (4), 2117–2133.

Huang, Y., Salama, Mhd.S., Krol, M.S., Su, Z., Hoekstra, A.Y., Zeng, Y., Zhou, Y., 2015. Estimation of human-induced changes in terrestrial water storage through integration of GRACE satellite detection and hydrological modeling: A case study of the Yangtze River basin. Water Resour. Res. 51, 8494–8516. https://doi.org/10.1002/2015WR016923.

Humphrey, V., Gudmundsson, L., Seneviratne, S.I., 2016. Assessing Global Water Storage Variability from GRACE: Trends, Seasonal Cycle, Subseasonal Anomalies and Extremes. Surv. Geophys. 37, 357–395. https://doi.org/10.1007/s10712-016-9367-1.

Humphrey, V., Zscheischler, J., Ciais, P., Gudmundsson, L., Sitch, S., Seneviratne, S.I., 2018. Sensitivity of atmospheric CO2 growth rate to observed changes in terrestrial water storage. Nature 560, 628–631. https://doi.org/10.1038/s41586-018-0424-4.

Jing, W., Zhao, X., Yao, L., Jiang, H., Xu, J., Yang, J., Li, Y., 2020. Variations in terrestrial water storage in the Lancang-Mekong river basin from GRACE solutions and land surface model. J. Hydrol. 580, 124258 https://doi.org/10.1016/j.jhydrol.2019.124258.

Johnston, R., Kummu, M., 2012. Water Resource Models in the Mekong Basin: A Review. Water Resour. Manag. 26, 429–455. https://doi.org/10.1007/s11269-011-9925-8.

Kingston, D.G., Thompson, J.R., Kite, G., 2011. Uncertainty in climate change projections of discharge for the Mekong River Basin. Hydrol. Earth Syst. Sci. 15, 1459–1471. https://doi.org/10.5194/hess-15-1459-2011.

Landerer, F.W., Flechtner, F.M., Save, H., Webb, F.H., Bandikova, T., Bertiger, W.I., Bettadpur, S.V., Byun, S.H., Dahle, C., Dobslaw, H., Fahnestock, E., Harvey, N., Kang, Z., Kruizinga, G.L.H., Loomis, B.D., McCullough, C., Murböck, M., Nagel, P., Paik, M., Pie, N., Poole, S., Strekalov, D., Tamisiea, M.E., Wang, F., Watkins, M.M., Wen, H.-Y., Wiese, D.N., Yuan, D.-N., 2020. Extending the global mass change data record: GRACE follow-on instrument and science data performance. Geophys Res Lett 47 (12). https://doi.org/10.1029/2020gl088306.

Lange, S., 2018. Bias correction of surface downwelling longwave and shortwave radiation for the EWEMBI dataset. Earth Syst. Dyn. 9, 627–645. https://doi.org/10.5194/esd-9-627-2018.

Lange, S., 2019. Trend-preserving bias adjustment and statistical downscaling with ISIMIP3BASD (v1.0). Geosci. Model Dev. 12, 3055–3070. https://doi.org/10.5194/gmd-12-3055-2019.

Li, F. Kusche, J. Chao, N. Wang, Z. Löcher, A. 2021. Long-Term (1979-Present) Total Water Storage Anomalies Over the Global Land Derived by Reconstructing GRACE Data. Geophys. Res. Lett. 48, e2021GL093492.

Liu, J., Chen, D., Mao, G., Irannezhad, M., Pokhrel, Y., 2022. Past and Future Changes in Climate and Water Resources in the Lancang-Mekong River Basin: Current Understanding and Future Research Directions. Engineering 13, 144–152.

Liu, B., Zou, X., Yi, S., Sneeuw, N., Cai, J., Li, J., 2021. Identifying and separating climate- and human-driven water storage anomalies using GRACE satellite data. Remote Sens Environ 263, 112559. https://doi.org/10.1016/j.rse.2021.112559.

Long, D., Longuevergne, L., Scanlon, B.R., 2014. Uncertainty in evapotranspiration from land surface modeling, remote sensing, and GRACE satellites. Water Resour. Res. 50 (2), 1131–1151.

Long, D., Pan, Y., Zhou, J., Chen, Y., Hou, X., Hong, Y., Scanlon, B.R., Longuevergne, L., 2017. Global analysis of spatiotemporal variability in merged total water storage changes using multiple GRACE products and global hydrological models. Remote Sens. Environ. 192, 198–216.

Mo, S., Zhong, Y., Forootan, E., Mehrnegar, N., Yin, X., Wu, J., Feng, W., Shi, X., 2021. Bayesian convolutional neural networks for predicting the terrestrial water storage anomalies during GRACE and GRACE-FO gap. J. Hydrol. 604, 127244.

Nagaraj, D., Proust, E., Todeschini, A., Rulli, M.C., D'Odorico, P.A., 2021. A new dataset of global irrigation areas from 2001 to 2015. 2021. A new dataset of global irrigation areas from 2001 to 2015. Adv. Water Res. 152 (2021), 103910.

Nie, J., Ruetenik, G., Gallagher, K., Hoke, G., Garzione, C.N., Wang, W., Stockli, D., Hu, X., Wang, Z., Wang, Y., Stevens, T., Danišík, M., Liu, S., 2018. Rapid incision of the Mekong River in the middle Miocene linked to monsoonal precipitation. Nat. Geosci. 11, 944–948. https://doi.org/10.1038/s41561-018-0244-z.

Oki, T., Kanae, S., 2006. Global hydrological cycles and world water resources. Science 313, 1068–1072. https://doi.org/10.1126/science.1128845.

Pech, S., Sunada, K., 2008. Population growth and natural-resources pressures in the Mekong River Basin. AMBIO 37 (3), 219–224.

Pham-Duc, B., Papa, F., Prigent, C., Aires, F., Biancamaria, S., Frappart, F., 2019. Variations of Surface and Subsurface Water Storage in the Lower Mekong Basin (Vietnam and Cambodia) from Multisatellite Observations. Water 11, 75. https://doi.org/10.3390/w11010075.

Pokhrel, Y., Felfelani, F., Satoh, Y., Boulange, J., Burek, P., Gädeke, A., Gerten, D., Gosling, S.N., Grillakis, M., Gudmundsson, L., Hanasaki, N., Kim, H., Koutroulis, A., Liu, J., Papadimitriou, L., Schewe, J., Müller Schmied, H., Stacke, T., Telteu, C.-E., Thiery, W., Veldkamp, T., Zhao, F., Wada, Y., 2021. Global terrestrial water storage and drought severity under climate change. Nat. Clim. Change 11 (3), 226–233.

Premoli, A., Tavella, P., 1993. A revisited three-cornered hat method for estimating frequency standard instability. IEEE Trans. Instrum. Meas. 42 (1), 7–13.

Reager, J.T., Famiglietti, J.S., 2009. Global terrestrial water storage capacity and flood potential using GRACE. Geophys. Res. Lett. 36, L23402.

Rodell, M., Famiglietti, J.S., Wiese, D.N., Reager, J.T., Beaudoing, H.K., Landerer, F.W., Lo, M.-H., 2018. Emerging trends in global freshwater availability. Nature 557 (7707), 651–659.

Save, H., Bettadpur, S., Tapley, B.D., 2016. High-resolution CSR GRACE RL05 mascons. J. Geophys. Res.-Solid. Earth 121, 7547–7569. https://doi.org/10.1002/2016JB013007.

Scanlon, B.R., Zhang, Z., Save, H., Wiese, D.N., Landerer, F.W., Long, D., Longuevergne, L., Chen, J., 2016. Global evaluation of new GRACE mascon products for hydrologic applications. Water Resour. Res. 52, 9412–9429. https://doi.org/10.1002/2016WR019494.

Scanlon, B.R., Zhang, Z., Save, H., Sun, A.Y., Müller Schmied, H., van Beek, L.P.H., Wiese, D.N., Wada, Y., Long, D.i., Reedy, R.C., Longuevergne, L., Döll, P., Bierkens, M.F.P., 2018. Global models underestimate large decadal declining and rising water storage trends relative to GRACE satellite data. Proc. Natl. Acad. Sci. U. S.A. 115 (6).

Schewe, J., Heinke, J., Gerten, D., Haddeland, I., Arnell, N.W., Clark, D.B., Dankers, R., Eisner, S., Fekete, B.M., Colón-González, F.J., Gosling, S.N., Kim, H., Liu, X., Masaki, Y., Portmann, F.T., Satoh, Y., Stacke, T., Tang, Q., Wada, Y., Wisser, D., Albrecht, T., Frieler, K., Piontek, F., Warszawski, L., Kabat, P., 2014. Multimodel assessment of water scarcity under climate change. Proc. Natl. Acad. Sci. U. S. A. 111, 3245–3250. https://doi.org/10.1073/pnas.1222460110.

Schmied, H.M., Caceres, D., Eisner, S., Floerke, M., Herbert, C., Niemann, C., Peiris, T.A., Popat, E., Portmann, F.T., Reinecke, R., Schumacher, M., Shadkam, S., Telteu, C.-E., Trautmann, T., Doell, P., 2021. The global water resources and use model WaterGAP v2.2d: model description and evaluation. Geosci. Model Dev. 14, 1037–1079. https://doi.org/10.5194/gmd-14-1037-2021.

Sun, Z., Long, D., Yang, W., Li, X., Pan, Y., 2020. Reconstruction of GRACE Data on Changes in Total Water Storage Over the Global Land Surface and 60 Basins. Water Resour. Res. 56 https://doi.org/10.1029/2019WR026250.

Tapley, B.D., Watkins, M.M., Flechtner, F., Reigber, C., Bettadpur, S., Rodell, M., Sasgen, I., Famiglietti, J.S., Landerer, F.W., Chambers, D.P., Reager, J.T., Gardner, A. S., Save, H., Ivins, E.R., Swenson, S.C., Boening, C., Dahle, C., Wiese, D.N., Dobslaw, H., Tamisiea, M.E., Velicogna, I., 2019. Contributions of GRACE to understanding climate change. Nat. Clim. Change 9, 358–369. https://doi.org/10.1038/s41558-019-0456-2.

Taube, C.M. 2000. Three Methods for Computing the Volume of a Lake. In J. C. Schneider (Ed.), Manual of fisheries survey methods II: with periodic updates. Michigan Department of Natural Resources, Fisheries Special Report. Chap. 12, pp. 175–179. Ann Arbor.

van den Broeke, M., Bamber, J., Ettema, J., Rignot, E., Schrama, E., van de Berg, W.J., van Meijgaard, E., Velicogna, I., Wouters, B., 2009. Partitioning Recent Greenland Mass Loss. Science 326, 984–986. https://doi.org/10.1126/science.1178176.

Västilä, K., Kummu, M., Sangmanee, C., Chinvanno, S., 2010. Modelling climate change impacts on the flood pulse in the Lower Mekong floodplains. J. Water Clim. Change 1, 67–86. https://doi.org/10.2166/wcc.2010.008.

Wang, Y.e., Feng, L., Liu, J., Hou, X., Chen, D., 2020. Changes of inundation area and water turbidity of Tonle Sap Lake: responses to climate changes or upstream dam construction? Environ. Res. Lett. 15 (9), 0940a1.
Wang, S., Zhang, L., She, D., Wang, G., Zhang, Q., 2021. Future projections of flooding characteristics in the Lancang-Mekong River Basin under climate change. J. Hydrol. 602, 126778.
Warszawski, L., Frieler, K., Huber, V., Piontek, F., Serdeczny, O., Schewe, J., 2014. The inter-sectoral impact model Intercomparison project (ISI–MIP): project framework Proc. Natl. Acad. Sci. 111 (9), 3228–3232.
Watkins, M.M., Wiese, D.N., Yuan, D.-N., Boening, C., Landerer, F.W., 2015. Improved methods for observing Earth's time variable mass distribution with GRACE using spherical cap mascons. J. Geophys. Res.-Solid. Earth 120, 2648–2671. https://doi.org/10.1002/2014JB011547.
Weedon, G.P., Balsamo, G., Bellouin, N., Gomes, S., Best, M.J., Viterbo, P., 2014. The WFDEI meteorological forcing dataset: WATCH Forcing Data methodology applied to ERA-Interim reanalysis data. Water Resour. Res. 50, 7505–7514. https://doi.org/10.1002/2014WR015638.
Wiese, D.N., Landerer, F.W., Watkins, M.M., 2016. Quantifying and reducing leakage errors in the JPL RL05M GRACE mascon solution. Water Resour. Res. 52, 7490–7502. https://doi.org/10.1002/2016WR019344.
Xie, J., Xu, Y.-P., Wang, Y., Gu, H., Wang, F., Pan, S., 2019. Influences of climatic variability and human activities on terrestrial water storage variations across the Yellow River basin in the recent decade. J. Hydrol. 579, 124218 https://doi.org/10.1016/j.jhydrol.2019.124218.
Xiong, J., Guo, S., Yin, J., Ning, Z., Zeng, Z., Wang, R., 2022. Projected changes in terrestrial water storage and associated flood potential across the Yangtze River basin. Sci. Total Environ. 817, 152998 https://doi.org/10.1016/j.scitotenv.2022.152998.
Yan, X., Zhang, B., Yao, Y.B., Yang, Y.J., Li, J.Y., Ran, Q.S., 2021. GRACE and land surface models reveal severe drought in eastern China in 2019. J. Hydr. 601, 126640.
You, Z., Feng, Z., Jiang, L., Yang, Y., 2014. Population distribution and its spatial relationship with terrain elements in Lancang-Mekong River Basin. J. Mountain Sci. 32 (1), 21–29 (in Chinese).
Yun, X., Tang, Q., Sun, S., Wang, J., 2021a. Reducing Climate Change Induced Flood at the Cost of Hydropower in the Lancang-Mekong River Basin. Geophys. Res. Lett. 48, e2021GL094243. https://doi.org/10.1029/2021GL094243.
Yun, X., Tang, Q., Li, J., Lu, H., Zhang, L., Chen, D., 2021b. Can reservoir regulation mitigate future climate change induced hydrological extremes in the Lancang-Mekong River Basin? Sci. Total Environ. 785, 147322 https://doi.org/10.1016/j.scitotenv.2021.147322.
Zhang, G., Yao, T., Shum, C.K., Yi, S., Yang, K., Xie, H., Feng, W., Bolch, T., Wang, L., Behrangi, A., Zhang, H., Wang, W., Xiang, Y., Yu, J., 2017. Lake volume and groundwater storage variations in Tibetan Plateau's endorheic basin. Geophys. Res. Lett. 44 (11), 5550–5560.
Zhang, G., Chen, W., Xie, H., 2019. Tibetan Plateau's Lake level and volume changes from NASA's ICESat/ICESat-2 and landsat missions. Geophys. Res. Lett. 46 (22), 13107–13118.
Zhang, G., Bolch, T., Chen, W., Crétaux, J.-F., 2021. Comprehensive estimation of lake volume changes on the Tibetan plateau during 1976–2019 and basin-wide glacier contribution. Sci. Total Environ. 772, 145463 https://doi.org/10.1016/j.scitotenv.2021.145463.
Zhong, Y., Feng, W., Humphrey, V., Zhong, M., 2019. Human-Induced and Climate-Driven Contributions to Water Storage Variations in the Haihe River Basin. China. Remote Sens. 11, 3050. https://doi.org/10.3390/rs11243050.
Zhu, E.D., Yuan, X., 2021. Global freshwater storage capability across time scales in the GRACE satellite era. Adv. Atmos. Sci. 38 (6), 905–917.